PHYSICAL REVIEW A VOLUME 57, NUMBER 6 JUNE 1998

Inner-shell photoionization of sodium: Experiment and theory

D. Cubaynes,[1] L. Voky,[2] F. J. Wuilleumier,[1] B. Rouvellou,[1] A. Hibbert,[3] P. Faucher,[2] J.-M. Bizau,[1] L. Journel,[1]
H. E. Saraph,[4] and F. Bely-Dubau[2]
[1]*Laboratoire de Spectroscopie Atomique et Ionique, Université Paris–Sud and URA 775 du CNRS, Batiment 350,*
91405 Orsay, France
[2]*URA 1362 du CNRS, Observatoire de la Côte d'Azur, Boîte Postale 229, 06304 Nice, France*
[3]*Queen's University of Belfast, Belfast BT7 1NN, United Kingdom*
[4]*University College London, London WC1E 6BT, United Kingdom*

(Received 30 December 1997)

Recent measurements of the photoionization of Na by ejection of a $3s$, $2p$, or $2s$ electron give branching ratios, β parameters, and absolute partial cross sections for a number of excitation processes, allowing one to perform the full partition of the total photoabsorption cross section into its components. In parallel, recent developments of the R-matrix code, together with extensive configuration and close-coupling expansions, make it possible to calculate the relevant quantities over the continuum energy range (40–140 eV) as well as in the resonant energy region corresponding to the excitation of a $2p$ or $2s$ inner-shell electron onto empty optical orbitals. A critical comparison is made of our experimental results with previous and present theoretical calculations. Valuable information is obtained for the ionization energies and relative cross sections. The main limitation in testing the validity of the various theoretical approximations is the lack of accuracy of the experimental photoabsorption cross section measured only to about 25%. [S1050-2947(98)06306-9]

PACS number(s): 32.80.Fb

I. INTRODUCTION

Characterization of the dynamics of the photon-atom interaction occurs through different parameters, which are primarily the partial photoionization cross sections and the angular distribution asymmetry parameters for all subshells involved in the photoionization process. The simplest systems, i.e., the closed-shell atoms, are now well understood. Many qualitative and quantitative results have been obtained for the rare gases and the agreement is good between theoretical calculations including electron correlation effects and the experimental data. The situation is more complex for open-shell atoms: The number of states resulting from multiplet splitting makes wave functions of high accuracy more difficult to obtain. On the experimental side, there are many fewer data available for metallic vapors than for the rare gases. In particular, absolute photoabsorption cross sections have been measured only for lithium [1], sodium [2], and barium [3] atoms.

Among all open-shell systems, the sodium atom with its $1s^2 2s^2 2p^6 3s$ electronic configuration occupies a special place in the Periodic Table. It is the first alkali-metal atom having a complete p subshell. Thus, with one excited electron outside of a closed core, it is possible to test certain classes of correlation effects that are not significant in the case of the rare gases. The sodium atom is light enough for extensive *ab initio* calculations to still be performed and heavy enough to have the binding energy of several inner subshells included in the photon energy range available, at our synchrotron radiation facility, for electron spectrometry studies. Thus absolute values of partial photoionization cross sections can be theoretically calculated and experimentally determined, providing a valuable test of the various theoretical approximations.

The experimental determination of accurate absolute values of partial photoionization cross sections is a difficult procedure. Using electron and ion spectrometries, it is possible to accurately measure *relative* intensities of the different photoionization processes. However, *absolute* values of the various cross sections cannot be measured with accuracy from the intensities of photoelectron lines because of too high uncertainties on the absolute values of some of the parameters involved in the experiments: The size of the interaction volume, the absolute density of the sample, the solid angle, and the efficiency of the detector. When one aims for 10–20 % accuracy one has to follow another method. Once branching ratios for all processes contributing to the total photoabsorption cross section are known, the absolute values of the partial cross sections can be determined by normalization to the measured photoabsorption cross section. Unfortunately, while absolute values of the total photoabsorption cross section are known within 2–3 % for the rare gases, this quantity has been measured to only 25% for the alkali-metal atoms [1,2] and recently to 15% for barium [3]. For all other atoms, absolute partial cross sections are determined by normalization to a theoretical calculation or by use of some sum rules that are not always accurate enough because one has to know all relative oscillator strengths and partial cross sections for resonant and continuum transitions over the whole photon energy range, respectively. Thus one is usually able experimentally to test only the *energy dependence* of theoretical calculations and not the absolute values of their results. Extensive tables for absolute values of partial cross sections exist only for helium and neon [4,5]. In the present work we have obtained the data to establish a similar table for atomic sodium.

In the case of sodium, the photoabsorption cross section has been measured in the 40–250 eV photon energy range to an accuracy of 20–25 % [2]. The previous work of Wolff *et al.* [6] did not involve determination of the absolute values

© 1998 The American Physical Society

of the total photoabsorption cross section. Some branching ratios for single [7,8] and double [9] photoionization processes have already been determined for up to 140 eV photon energy. More accurate measurements are presented in this paper. Combining all experimental data, it was possible to determine the *absolute values of each partial photoionization cross section* and to compare them directly with theory.

Measurements of the angular distribution of photoelectrons do not require the knowledge of any absolute cross section. However, accurate measurements of the relative intensity of photoelectrons ejected at various azimuthal angles must be performed in exactly the same experimental conditions. In the work presented here, we used a multichannel detection device to measure the angular distribution parameter β of the photoelectrons ejected from the $2p$ subshell of atomic sodium for the single photoionization process ($2p$ main line) and for simultaneous excitation and ionization processes (correlation satellites).

On the theoretical side, the total $2p$ cross section, excluding the resonance structure, was calculated with a very simple theoretical one-electron model many years ago [10]. Soon after, a highly correlated model, the random-phase approximation with exchange (RPAE) that includes intra- and intershell correlations, was used by Amusia *et al.* [11–13] to calculate the $2p$ and $3s$ total cross sections; in the same work, a comparison was also made with the results of Hartree-Fock calculations (these results are labeled HF_1L and HF_1V in the following). Some years later, calculations for the $2p$ and $2s$ photoionization cross sections were carried out [14] using both Hartree-Slater (HS) and Hartree-Fock approximations (HF_2L and HF_2V). When experimentalists succeeded in measuring correlation satellites by using photoelectron spectrometry [15], calculations that were able to calculate separately partial subshell photoionization cross sections and to determine angular distribution parameters were called for. Chang and Kim [16] used many-body perturbation theory (MBPT) to calculate the partial cross sections and the asymmetry parameter β for $2p$ subshell photoionization (MBPT-1). Isenberg *et al.* [17] had some success interpreting the observed resonance structure; they also calculated partial cross sections. In their MBPT calculations, they used a limited close-coupling expansion (MBPT-2). Craig and Larkins [18] used a relaxed Hartree-Fock (RHF) model to calculate partial cross sections and asymmetry parameters. Msezane, Armstrong-Mensah, and Niles [19] and Tayal, Msezane, and Manson [20] used the R-matrix method [21], but due to shortcomings in their target state expansion their results are in poor agreement with experiment. Their calculations indicate the sensitivity of the calculated resonance positions to the target state representation. Most recently, two theoretical papers using many-body perturbation theory by Liu and Liu [22] (MBPT-3) and a multiconfiguration Hartree-Fock (MCHF) approach by Saha [23] have presented partial cross sections and angular distribution of the photoelectrons.

In our R-matrix calculations covering an extended photon energy range (26–140 eV), it is necessary to employ a sufficiently large close-coupling (CC) expansion to obtain a complete model of the physical process over a wide range of energies. The CC development is *ab initio* and it automatically yields complete series of resonance states converging on all ion terms included in the expansion. In particular, the full channel coupling describes such processes as shake-up (SU), where the ion is left in an excited state of the same parity, and ''conjugate shake-up'' (CSU), where the excited ionic state has the opposite parity to that of the ionic state $1s^22s^22p^53s\ ^{1,3}P_0$. The accuracy with which the position of these resonances are calculated depends crucially on two criteria. First, the model ion must be such that the experimental energies of all target states that are included in the CC expansion match the experimental energies very closely. In the case of the present Na^+ target, this meant that all terms lying between $1s^22s^22p^6\ ^1S$ and $1s^22s2p^64d\ ^1D$, spanning 5.6 Ry, had to be accurately represented using the same orbitals and configurations throughout. Second, the CC expansion and the complementary expansion over $(N+1)$-electron ''bound states'' must be consistent. The target spans an energy range that includes infinitely many terms converging on the $2s^22p^5\ ^{1,3}P$ and $2s2p^63s\ ^{1,3}S$ ionization thresholds of Na^+. Consequently, inner-shell photoionization calculations in the CC approximation that include all the details presented here are only possible by carefully choosing a representative set of target terms. The selected CC channels must be matched by a corresponding choice of $(N+1)$-electron bound-state configurations [24].

Our work is presented as follows. The experimental procedure and data analysis are described in Sec. II. The target calculation and the details of the configuration-interaction (CI) expansion and of the CC problem using the R-matrix method are described in Sec. III. Theoretical and experimental results for the partial cross sections and angular distribution parameters are presented and compared in Sec. IV. Conclusions are given in Sec. V.

II. EXPERIMENT

The experimental data determined in this work have been obtained using electron spectroscopy and the synchrotron radiation (SR) emitted by a bending magnet of the Super-ACO (Anneau de Collisions d'Orsay) storage ring over the photon energy range extending from 20 to 140 eV. Previously, the experimental design has been described only briefly [7]. Here we will give more details about the experimental setup and procedure.

A. Experimental setup

The whole experimental setup is shown in Fig. 1. SR emitted in the bending magnet is focused on the entrance slit of the monochromator with a toroidal mirror, after deflection in the horizontal plane by a plane mirror. The entrance and exit slits of the monochromator are adjustable under vacuum. Dispersion of the light is achieved by a toroidal holographic grating under grazing incidence. Two gratings are permanently mounted in the grating holder: The first grating is etched to 450 lines/mm and is blazed at a photon energy of 35 eV; the second one is etched to 1200 lines/mm and optimized for photon energies higher than 90 eV. After the exit slit, the beam is refocused onto the source volume of an electron analyzer by a second toroidal mirror. A gold mesh is placed in the photon beam to measure continuously the pho-

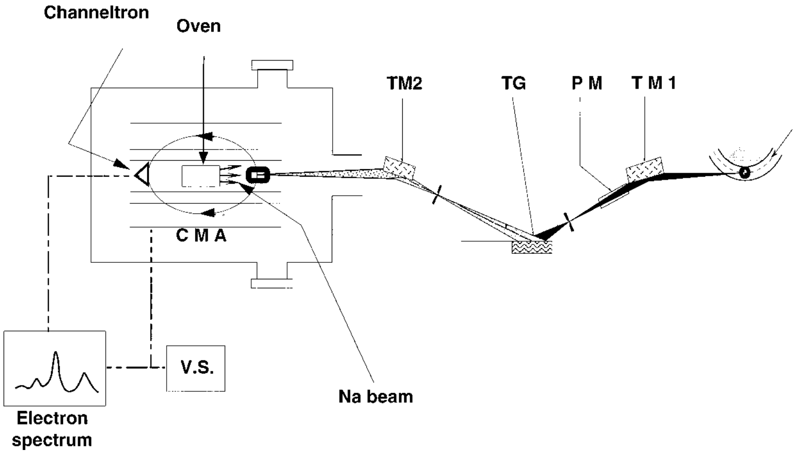

FIG. 1. Experimental setup: TM_1 and TM_2 toroidal mirrors; PM, plane mirror; TG, toroidal grating; CMA, cylindrical mirror analyzer. The channeltron is located on the axis of the CMA and collects all photoelectrons emitted from the source volume at the magic angle $\theta = 54°44'$.

ton flux. Typically, about 10^{12} photons/sec are available in the interaction region at 35 eV photon energy with 500-μm slits (relative bandwidth $\Delta\lambda/\lambda = 1\%$) and 400 mA positron beam current.

The electron spectrometer is a cylindrical mirror analyzer (CMA) composed of three cylinders. To be able to vary the size of the source volume as well as the resolution of the analyzer, the CMA was designed with two inner cylinders and four adjustable entrance and exit slits. With 4 mm slit widths, the resolution of the analyzer is 0.85% and 1.25% of the electron pass energy for angle-integrated and angle-resolved measurements, respectively. The inner cylinders are grounded and the analyzing voltage is applied to the outer cylinder.

In order to evaporate the atomic sodium, a stainless-steel furnace is mounted on the axis of the CMA. It is resistively heated by a Ni-Cr thermocoax. A thermocouple is used to monitor the temperature. A liquid-nitrogen-cooled finger is located in the CMA very close to the source volume and serves to trap the sodium atoms after the interaction region. The oven can be used for two days before a refilling is needed. It emits an effusive beam of sodium atoms that is collinear to the photon beam. The maximum atomic density used in our experiments was limited to $10^{12}-10^{13}$ atoms/cm^3 in order to minimize the effect of inelastic scattering of the photoelectrons.

The experiment was originally designed to measure relative partial cross sections in using the photon beams emitted from bending magnets [25]. Then the axis of the CMA was chosen to be collinear with the photon beam because of the elliptical polarization of SR since it is well known that the radiation emitted from a bending magnet is elliptically polarized with a linear polarization rate on the order of 60–70 %. In the nonrelativistic dipole approximation, which is valid at the low photon energies investigated in this work, the differential photoionization cross section $d\sigma_{nl}/d\Omega$ for (n,l) atomic electrons in the $d\Omega$ solid angle is given, for an elliptically polarized photon beam and a randomly oriented target, by [26,27]

$$d\sigma_{nl}/d\Omega = \sigma_{nl}/4\pi\{1-\beta_{nl}/2[P_2(\cos\theta) - \tfrac{3}{2}p\,\sin^2\theta\cos 2(\varphi+\varphi_0)]\}, \qquad (1)$$

with P_2 the Legendre polynomial of second order; p the rate of linear polarization of the monochromatized radiation equal to $\cos 2\omega$, where ω is the ellipticity of the polarization ellipse $\omega = \arctan(b/a)$, b and a being the length of the small and large axes of the ellipse, respectively; θ the angle between the directions of photons and photoelectrons; $\varphi+\varphi_0$ the azimuthal angle of the photoelectrons referred to the main electrical vector of the radiation, i.e., the main axis of the polarization ellipse; φ and φ_0 defined in Fig. 2, where the setup for the angular distribution measurements (to be described later) is schematically illustrated; β_{nl} the asymmetry parameter characterizing the angular distribution of the photoelectrons emitted from the (n,l) subshell; and σ_{nl} the partial cross section for photoionization of electrons from the (n,l) subshell. Collecting all photoelectrons emitted in the angular range $0 \leqslant \varphi \leqslant 2\pi$ and choosing $\theta = 54°44'$ (the magic angle) makes the differential photoionization cross section equal to

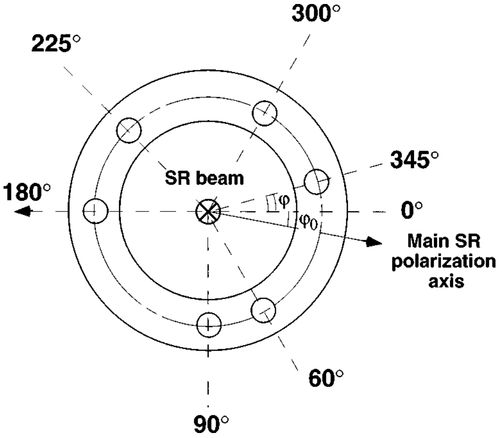

FIG. 2. Geometry of the experimental setup for angle-resolved experiments in a plane perpendicular to the CMA axis.

$$d\sigma_{nl}/d\Omega=\sigma_{nl}/4\pi \tag{2}$$

since, by integration over φ in the angular range $(0,2\pi)$, the term depending on φ cancels.

For angle-integrated measurements of partial cross sections, the electrons emitted from the extended source volume of the CMA are energy analyzed and counted by one channeltron located on the CMA axis, as it is shown in Fig. 1. In this geometry, the electron signal is proportional to the differential cross section and then to the subshell cross section according to relation (2).

For angle-resolved experiments several identical channeltrons, six in the work presented here, are mounted along a ring coinciding with the first-order focus located between the two inner cylinders, as it is illustrated in Fig. 2. The angular position of each channeltron is determined by the angle φ that is the angle between the direction of the outgoing electrons on a plane perpendicular to the CMA axis and the horizontal axis. Values of φ chosen for these measurements are indicated in Fig. 2. The angular acceptance of each channeltron is here $\Delta\varphi=\pm 8°$. Since the polarization ellipse, initially in the horizontal plane of the positron orbit in the storage ring, rotates under reflection on the various optical elements in the beam line, the rotation angle φ_0 must be measured for angular distribution studies. The great advantage of this multidetection system is that it is possible to measure the emitted electron intensity simultaneously at several φ angles. This decreases the acquisition time and cancels errors due to possible unstabilities in the atomic beam density or photon beam intensity.

The number of electrons $N(\varepsilon,\varphi)_{nl}d\varepsilon$ emitted from the (n,l) subshell by an incoming photon flux $N(h\nu)d(h\nu)$ in the energy interval $d(h\nu)$ and detected in the aperture angle $2\Delta\varphi$ by one channeltron located at the angle φ and at $\theta=54°44'$ is given by

$$\begin{aligned}N_{nl}(\varepsilon,\varphi)d\varepsilon=&G\rho L\,\eta(\varepsilon)T(\varepsilon,\varphi)N(h\nu)\sigma_{nl}(h\nu)\\&\times\{1+0.494\beta_{nl}(h\nu)p(h\nu)\\&\times\cos 2[\varphi+\varphi_0(h\nu)]\}\Delta\varphi d(h\nu),\end{aligned} \tag{3}$$

with G the constant value including a geometrical factor, ρ the atomic density in the source volume, L the length of the source volume, η (ε) the efficiency of the channeltron for electrons with energy ε, and $T(\varepsilon,\varphi)$ the transmission of the CMA for electrons emitted at the angle φ with energy ε. The signal issued from the channeltron(s) enters one (or six) counters after amplification and discrimination. Two calibrated Hewlett-Packard voltage sources are used to establish the analyzing voltage. The whole experiment is driven by a HP-9000 computer. It controls the voltage sources, the counters, and the Keithley ammeter plugged to the gold mesh placed in the photon beam and drives the monochromator.

B. Experimental procedure for partial-cross-section determination

1. Photoelectron spectra

For partial-cross-section measurements on a relative scale, the experimental setup shown in Fig. 1, i.e., with one channeltron located on the axis of the CMA, allows us to get the most accurate data. We show in Fig. 3 a typical electron spectrum produced by photoionization of atomic sodium in the $2p$ subshell with 75.6-eV photons. On the upper horizontal axis, the binding-energy scale has been determined by the simple energy conservation rule, knowing the photon energy and the contact potentials from calibration measurements. The kinetic energy of the electrons can be determined with our setup to within 0.01–0.05 eV, depending on the kinetic-energy range. Each photoelectron peak corresponds to a specific final state of the Na$^+$ ion that can be reached by photoionization: main lines due to single photoionization of sodium atoms in the $2p$ subshell (at 38.04 and 38.46 eV binding energies, final states $2s^22p^53s$ $^1P_1$ and $^3P_{0,1,2}$, respectively), correlation satellites at higher binding energies, e.g., shake-up satellites near 46 eV binding energy (final ionic states $2s^22p^54s$ $^{1,3}P$), and conjugate shake-up or "knock out" [28] satellites around 42 eV binding energy (final ionic states $2s^22p^53p$ $^{1,3}L$). Other correlation satellites of weaker intensities are observed at higher binding energies. Throughout the following sections, we will use the terms main line (ML), shake-up satellites, and conjugate shake-up satellites to refer to these various categories of electron lines.

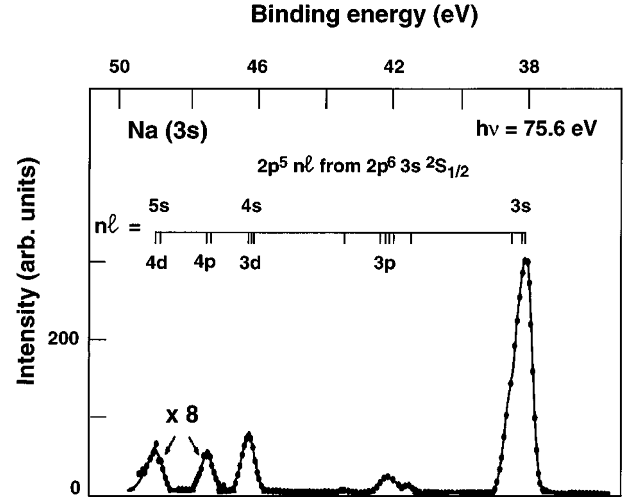

FIG. 3. Photoelectron spectrum of atomic sodium taken at $h\nu=75.6$ eV. The electron line at 38 eV binding energy is due to single photoionization of the $2p$ electrons. The other group of lines at higher binding energies are satellite lines: $2p^53p$ and $2p^54p$ CSU lines, around 42 and 47 eV, respectively; $2p^54s$ and $2p^55s$ SU lines near 46 and 49 eV, respectively. Peaks corresponding to $2p^53d$ and $2p^54d$ final ionic states are not resolved from peaks corresponding to $2p^54s$ and $2p^55s$, respectively.

The electronic configuration of the various final states are marked by vertical bars in Fig. 3. The experimental binding energies are in accordance with the detailed term values as given by Moore [29].

2. Branching ratios and relative photoionization cross sections

For angle-integrated spectra, i.e., for spectra integrating electrons emitted in the $(0,2\pi)$ φ angular range at $\theta=54°44'$, such as the one shown in Fig. 3, relation (3) becomes

$$N_{nl}(\varepsilon)=C\,\eta(\varepsilon)T(\varepsilon)N(h\nu)\sigma_{nl}(h\nu), \tag{4}$$

with $C=G\rho L/4\pi$. As already mentioned in the Introduction, absolute determinations of $\sigma_{nl}(h\nu)$ from relation (4) would require accurate absolute measurements of $T(\varepsilon)$, $\eta(\varepsilon)$, and the various factors included in the constant C. The main difficulty in electron spectrometry is to accurately determine the absolute atomic density and the actual size of the source volume ''seen'' by the detector in the electron spectrometer. This is not possible when one aims at a 25% accuracy. However, for a comparison of the various $\sigma_{nl}(h\nu)$ corresponding to several final ionic states observed in the *same* electron spectrum as described above, *accurate branching ratios*, typically within 1% and 3–5% for high- (above 10 eV) and low- (3–10 eV) kinetic-energy electron lines, respectively, can be obtained by comparing the $N_{nl}(\varepsilon)$ integrated area of the observed electron peaks. Then, at a given $h\nu$ photon energy, partial cross sections can be compared from the measured branching ratios using expression (4). For all electron lines in an electron spectrum, C and $N(h\nu)$ keep the same values. η (ε) is also the same, provided a high-enough post-acceleration voltage (60–80 V) is applied to the grid placed in front of the channeltron. Thus, comparing two cross sections $\sigma_{n_1l_1}$ and $\sigma_{n_2l_2}$ from the integrated area of the corresponding electron lines with kinetic energies ε_1 and ε_2 requires the knowledge, on a *relative* scale, of the $T(\varepsilon)$ CMA transmission function, according to the relation

$$\sigma_{n_1l_1}(h\nu)/\sigma_{n_2l_2}(h\nu)=[N_1(\varepsilon_1)/N_2(\varepsilon_2)][T(\varepsilon_2)/T(\varepsilon_1)]. \tag{5}$$

In the constant resolution mode of the CMA used throughout these experiments, i.e., with variable transmission energies, the transmission of the analyzer is proportional to the kinetic energy of the electrons at sufficiently high kinetic energy, above typically 10–15 eV, but not at lower kinetic energies. So we used two different procedures to determine $T(\varepsilon)$. First, the intensity ratio between the electron line produced by photoionization of a core electron and one of the Auger lines due to relaxation of this core hole must be constant when one varies the photon energies (but, possibly, over some specific and narrow energy ranges [30]). Thus, by varying systematically the photon energy and then the kinetic energy of the photoelectrons, $T(\varepsilon)$ was determined on a relative scale by measuring the integrated area under the photoelectron and Auger lines, respectively. In applying this procedure, one has to be sure that only photons diffracted in the first order by the monochromator contribute to the formation of the core holes. This condition was easily fulfilled by choosing the Auger lines emitted in the relaxation of a $3d$ hole in krypton. The binding energy of these $3d$ electrons, and thus the lowest photon energy needed in this calibration procedure, is 93 eV. Since the cutoff energy of the beam line is 160 eV, we had no contribution from photons diffracted in higher orders.

A second method was to follow the variation of the relative intensity of the Ne $2p$ photoelectron line as a function of the kinetic energy of the electrons, using the relative variation of the photon flux as measured by the gold mesh and the nanoammeter. Since the binding energy of these electrons is 21.59 eV, higher-order photons contribute to the reading of the nanoammeter and their relative contribution should be removed. Photoelectrons emitted from the $2p$ subshell of neon by the photons diffracted in various orders, up to the sixth order, were measured and the known $2p$ photoionization cross section [4,5] was used to correct the relative variation of the photon flux. The energy dependence of the photoyield of gold was taken from the measurements of Ederer [31]. This second method was an iterative method and the procedure was applied several times at each photon energy.

Results obtained in both methods were in good agreement. Alternatively, once the transmission curve of the CMA was well known, measuring the energy variation of the neon $2p$ photoelectron line produced by first-order photons offered often a more accurate way to determine the relative variation of the photon flux than to correct the current from the gold mesh. This possibility has been used especially to normalize the relative data obtained in the resonant energy region of the spectrum. Let us mention also that the measurement of the neon $2p$ photoelectron line diffracted in several orders by the monochromator serves to check accurately, within 0.02 eV usually, the energy of the monochromator. In any case, since the transmission of the CMA in the constant resolution mode is continuously decreasing with decreasing kinetic energies (down to zero at about 3 eV), the accuracy is lower (3–5%) in our determinations of branching ratios involving electron lines with kinetic energies below 10 eV (in the 3–10 eV energy range) than in the range of higher kinetic energies (2–3%).

3. Absolute values of the partial cross sections

Branching ratios for photoionization into the various continuum channels were determined over the whole photon energy range as described in the preceding paragraph. To obtain the absolute values of the partial cross sections, two methods can be used. First, once all branching ratios have been measured using electron and ion spectrometries, one can normalize the data at one photon energy to the measured absolute photoabsorption cross section and measure, with the electron analyzer, the relative variation of one photoelectron line as a function of the photon energy. Second, one can normalize the relative values of the partial cross sections resulting, at each photon energy, from the previous partitioning of the total cross section to the absolute value of the measured total cross section. We have chosen the second solution to obtain the absolute values of the partial cross sections presented in the following sections, except in the scanning of the 64–72 eV resonance region where the first solution has been adopted.

C. Angular distribution measurements

For angular distribution measurements, the six channeltrons record simultaneously electrons emitted at the φ angles indicated in Fig. 2. An example of the six angle-resolved photoelectron spectra measured at 105 eV photon energy is shown in Fig. 4. The angle-resolved integrated area under each photoelectron line measured by each channeltron i at the angle φ_i is proportional to the angle-resolved cross section $\sigma(\varphi_i)$, which is obtained from a double integration over θ and φ of the differential equation (1), according to

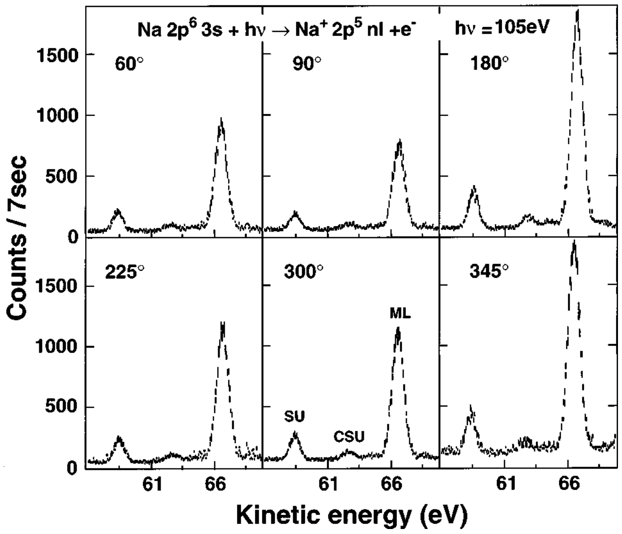

FIG. 4. Angle-resolved electron spectra taken at $h\nu=105$ eV for six different values of the angle φ.

$$\sigma(\varphi_i)=\sigma/4\pi\int_{\varphi_i-\Delta\varphi}^{\varphi_i+\Delta\varphi}\delta\varphi\int_{\theta_{\min}}^{\theta_{\max}}\sin\,\theta\;d\theta\{1-\beta_{nl}/2$$

$$\times[P_2(\cos\,\theta)-\tfrac{3}{2}p\,\sin^2\,\theta\,\cos 2(\varphi_i+\varphi_0)]\},\quad(6)$$

where φ_i is the azimuthal angle corresponding to the mean position of each channeltron i and $\Delta\varphi$ is half the angular aperture of them.

The cylindrical symmetry of the CMA makes easy the integration over φ if one considers in the first approximation the source volume as a point source and neglects a possible spiraling of the electrons around the CMA axis (this effect would lead to detecting electrons emitted at other values of the φ angle, but it is negligible in our cases [32]). The integration over θ is more complicated. Taking into account the effective size of the source volume and the influence of the finite acceptance angle of the spectrometer as described in Ref. [32], one obtains the final expression for $\sigma(\varphi_i)$ to be used in analyzing the angle resolved data:

$$\sigma(\varphi_i)=C\sigma[1+0.494\beta p\;\cos 2(\varphi_i+\varphi_0)].\quad(7)$$

Replacing in Eqs. (3) and (7) $CG\rho L\eta(\varepsilon)N(h\nu)$ by a constant C', the angle-resolved number of counts in the angular aperture $2\Delta\varphi$ can be expressed as

$$N_{nl}(\varepsilon,\varphi_i)=C'\sigma_{nl}(h\nu)[1+0.494\beta_{nl}(h\nu)p(h\nu)$$

$$\times\cos 2[\varphi_i+\varphi_0(h\nu)]]T(\varepsilon,\varphi_i).\quad(8)$$

Calibration of the relative transmissions $T(\varepsilon,\varphi)$, the rate of linear polarization p of SR, and the rotation angle φ_0 was achieved by measuring the well-known angular distribution of the photoelectrons emitted from rare-gas atoms (He $1s$ and Ar $3p$ photolines). The $4d^95s^25p^6\;{}^2D_{5/2}\rightarrow4d^{10}5s^25p^4\;{}^1S_0+e^-$ Auger line of xenon was also used. Internal calibration in every photoelectron spectrum of sodium was also checked by using the $2s$ or $3s$ photoelectron lines of sodium whose asymmetry parameters β were calculated in a Dirac-Fock approximation to be equal to 2 well above the threshold [33,34]. In order to obtain β, we evaluated the integrated area under each photoelectron line $N_{nl}(\varepsilon,\varphi_i)$ and fitted formula (8) to the data by using β as a free parameter. As an example, we show in Fig. 5 the measured angular distribution (at 105 eV) of the CSU photoelectron line. The solid line represents the fit with a β value of 0.72 using the measured values of p and φ_0 ($p=0.62\pm0.02$ and $\varphi_0=5.7°\pm0.3°$). The uncertainty on this value of β is ±0.13.

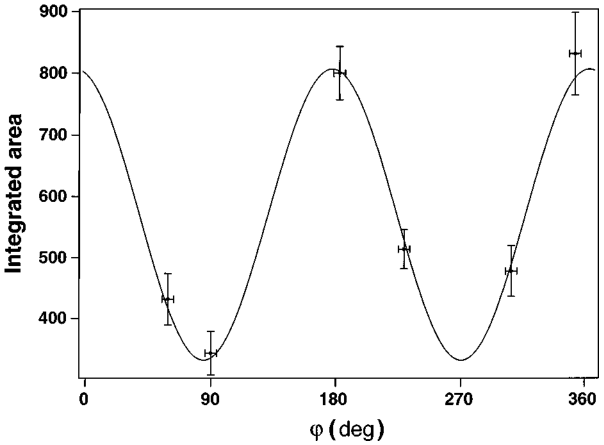

FIG. 5. Angle-resolved measurements for the intensity of the first CSU line measured at various φ angles at $h\nu=62$ eV. The solid line is the result of the fitting procedure according to Eq. (8).

III. THEORY

A. Na$^+$ target wave functions

In recent calculations of wave functions, energies, and oscillator strengths for the neon isoelectronic sequence [35], the energies for $n=3$ levels were optimized. In the present work it was necessary to optimize all targets states $2s^22p^5nl$ and $2s2p^6nl$, with $n=3$ and 4. Starting with the radial functions as obtained in the paper on the neon sequence and using the code CIV3 by Hibbert [36], a set of optimized radial functions was calculated.

1. Target orbitals

The radial functions are expressed as Slater-type orbitals

$$P_{nl}(r)=\sum_{j=1}^{k}C_{jnl}\left[\frac{(2\zeta_{jnl})^{2I_{jnl}+1}}{(2I_{jnl})!}\right]^{1/2}r^{I_{jnl}}\exp(-\zeta_{jnl}r).\quad(9)$$

The parameters for the $1s$ and $2s$ orbitals were taken from the compilation of Clementi and Roetti [37] for the $1s^22s^22p^5\;{}^2P^o$ state of Na^{2+}. The parameters for all other target orbitals were optimized as shown in Table I. The $n=3$ and 4 orbitals were chosen to be spectroscopic so that they describe the outermost electrons in each state, while the $5s$, $5p$, and $5d$ functions are "correlation" orbitals, chosen to improve the ground-state representation. In particular, the $2p$ function of the Na^{2+} ion is somewhat different from that for the $2p^6$ Na$^+$ ground state; the $5p$ function acts as a correcting function. The $5s$ orbital plays the same role with respect to the $2s$ orbital, although the difference between the $2s$ functions for the different states is not so great. In our earlier work [38] it was found that the major correlation ef-

TABLE I. Method of optimization for the Na^+ orbitals.

Orbital	Energy functional optimized
$1s,2s$	$1s,2s$ of Na^{2+}: $1s^22s^22p^5\,P^{o}$ [a]
$2p$	$2p^53s\ ^3P^o$
$3s$	average (equally weighted) of $2p^53s\ ^{1,3}P^o$
$4s$	average (equally weighted) of $2p^54s\ ^{1,3}P^o$ with configurations $2p^53s,\ 2p^54s$
$3p$	average (equally weighted) of $2p^53p\ ^3S,{}^{1,3}P,{}^{1,3}D$
$4p$	average (equally weighted) of $2p^54p\ ^3S,{}^{1,3}P,{}^{1,3}D$ with configurations $2p^53p,\ 2p^54p$
$3d$	average (equally weighted) of $2p^53d\ ^{1,3}P^o,{}^{1,3}D^o,{}^{1,3}F^o$
$4d$	average (equally weighted) of $2p^54d,{}^{1,3}P^o,{}^{1,3}D^o,{}^{1,3}F^o$ with configurations $2p^53d,\ 2p^54d$
$4f$	average (equally weighted) of $2p^54f,{}^{1,3}F$
$\overline{5s}$	$2p^6\ ^1S$ with configurations $2p^6,2p^5np,2s2p^6ns$ $(n=3,4,\overline{5})$
$\overline{5p}$	$2p^6\ ^1S$ with configurations $2p^6,\ 2p^5np$ $(n=3,4,\overline{5})$
$\overline{5d}$	$2s^22p^63s\ ^1S$ with configurations $2p^6,2p^5np,2s2p^6ns,2s^22p^43snd$ $(n=3,4,\overline{5})$

[a] From Ref. [37].

fect in the $2s2p^6nl$ states can be included by means of the configuration $2s^22p^4\overline{5d}nl$ and the present $\overline{5d}$ function is optimized to account for this. The optimized parameters can be given upon request.

2. Wave functions and energies

The 29 basic configurations used for building the 39 target states are listed in Table II. The configurations marked with an asterisk were included only for states of ^1S symmetry where they serve to correct for the differences between the $2s$ and $2p$ orbitals of the ground state and those of the higher states. In addition, they serve to add sufficient correlation effects to bring the energy separations between the ground state and the core excited states into close agreement with experiment. The remaining 23 configurations give rise to 258 symmetries when all angular momentum couplings are accounted for. All 264 configurations were employed to build the 39 target states that were retained in the CC expansion.

TABLE II. Configurations used in Na^+ target states. An asterisk denotes for ^1S symmetry only.

14 basic spectroscopic configurations
    $1s^22s^22p^6$
    $2p$ injection
    $[1s^2]2s^22p^53s,2s^22p^53p,2s^22p^53d,2s^22p^54s,$
    $2s^22p^54p,2s^22p^54d,2s^22p^54f$
    $2s$ injection
    $[1s^2]2s2p^63s,2s2p^63p,2s2p^63d,$
    $2s2p^64s,2s2p^64p,2s2p^64d$

15 correlation configurations
    $2p$ injection
    $[1s^2]2s^22p^5\overline{5p}*,2s^22p^43s\overline{5d},2s^22p^43p\overline{5d},$
    $2s^22p^43d\overline{5d},2s^22p^44s\overline{5d},2s^22p^44p\overline{5d},$
    $2s^22p^44d\overline{5d},2s^22p^44f\overline{5d},2p^6\overline{5s}^2*,\ 2p^65p^2*,2p^6\overline{5d}^2*$
    $2s$ injection
    $[1s^2]2s2p^6\overline{5s},2s2p^6\overline{5p},$
    $2s2p^5\overline{5s}\,\overline{5p}*,2s2p^5\overline{5p}\,\overline{5d}*$

TABLE III. Target state energies relative to the $1s^22s^22p^6\ ^1S$ ground state of Na ($E=-161.730\,306$ a.u.). The first thresholds are for $2p^53s\ ^{1,3}P^o$, 38.46 and 38.06 eV (calc.) and 38.46 and 38.04 eV (expt.). The second thresholds for $2s2p^63s\ ^{1,3}S^e$, 70.38 and 70.97 eV (calc.) and 71.3 and 70.9 eV (expt.).

Term	State	This work (cm^{-1})	Expt.[a,b] (cm^{-1})
1	$2p^6\ ^1S$	0	0
2	$2p^53s\ ^3P^o$	265 490	265 377
3	$2p^53s\ ^1P^o$	268 795	268 623
4	$2p^53p\ ^3S$	293 290	293 220
5	$2p^53p\ ^3D$	297 478	297 615
6	$2p^53p\ ^1D$	299 110	299 027
7	$2p^53p\ ^1P$	299 790	300 100
8	$2p^53p\ ^3P$	299 825	300 200
9	$2p^53p\ ^1S$	309 433	308 861
10	$2p^53d\ ^3P^o$	330 056	330 713
11	$2p^54s\ ^3P^o$	331 004	331 904
12	$2p^53d\ ^1P^o$	331 133	331 745
13	$2p^53d\ ^1D^o$	331 531	332 800
14	$2p^53d\ ^3D^o$	331 531	332 900
15	$2p^54s\ ^1P^o$	331 764	332 691
16	$2p^54p\ ^3S$	339 596	
17	$2p^54p\ ^3D$	340 732	
18	$2p^54p\ ^1D$	341 265	
19	$2p^54p\ ^1P$	341 426	
20	$2p^54p\ ^3P$	341 439	
21	$2p^54p\ ^1S$	345 915	
22	$2p^54d\ ^3P^o$	352 329	
23	$2p^54d\ ^1P^o$	352 832	
24	$2p^54d\ ^1D^o$	352 862	
25	$2p^54d\ ^3D^o$	352 862	
26	$2p^54f\ ^3D^o$	352 862	
27	$2p^54f\ ^1D$	352 913	
28	$2s2p^63s\ ^3S$	531 047	530 690[b,c]
29	$2s2p^63s\ ^1S$	534 387	533 872[b,c]
30	$2s2p^63p\ ^3P^o$	562 430	562 800
31	$2s2p^63p\ ^1P^o$	564 132	564 210
32	$2s2p^63d\ ^3D$	594 744	
33	$2s2p^64s\ ^3S$	594 810	
34	$2s2p^63d\ ^1D$	594 916	
35	$2s2p^64s\ ^1S$	595 525	
36	$2s2p^64p\ ^3P^o$	604 724	
37	$2s2p^64p\ ^1P^o$	605 304	
38	$2s2p^64d\ ^3D$	616 342	
39	$2s2p^64d\ ^1D$	616 440	

[a] Reference [39], quoting from Ref. [40].
[b] Weighted average of J levels, with an estimate of the effect of mixing of LS levels for a particular J removed.
[c] Present work.

The list of these 39 target states is given in Table III in which our theoretical separations are compared with existing experimental values. In general, the agreement between our calculation and experiment is good; most differences are less than 1000 cm^{-1} (i.e., 0.1 eV or about 0.5%). For a meaningful comparison the ''experimental'' term energies in LS coupling are obtained from the J-dependent experimental level energies by taking the weighted mean and also accounting for coupling between different LS terms sharing a common J. Note in particular the good agreement for states with configuration $2s2p^63s$.

B. The scattering calculation

1. The wave function for the (N+1)-electron system

A detailed discussion of the R-matrix method as used for the calculation of inner-shell photoionization processes has already been given elsewhere [24]. Wave functions for the target plus electron system [the $(N+1)$-electron state] are required for the ground state of sodium and for the continuum states. The wave function for the $(N+1)$-electron system of total symmetry $SL\pi$ is given by

$$\Psi^{SL\pi}=A\sum_{i}^{N_F}\ \Phi_i(S_iL_i;x_1,\ldots,x_N,\hat{x}_{N+1})\times F(k_il_i;r_{N+1})r_{n+1}^{-1}+\sum_{j}^{N_B}\ c_j\Phi_j^{Sl\pi}, \tag{10}$$

where the Φ_i are the CI wave functions of the target terms that have been included in the CC expansion and they are coupled to the angular and spin coordinates of the additional electron. The Φ_j in the second sum represent $(N+1)$-electron states made up entirely of target orbitals. These are also referred to as bound states in this paper. In order for the CC expansion to be consistent the sum over Φ_j must include all $(N+1)$-electron states that have exactly N-electron parent terms included in the first summand. The energy range covered by the selected target states spans two subshell ionization thresholds. We chose not to include target states $2p^5nl$ with principal quantum numbers $n>4$, although we had target configurations that included orbitals with principal quantum number $n=5$. The omission of target terms belonging to configurations included in the CI expansion and lying within the energy range of the close-coupling expansion necessitated a matching selection of configurations for the $(N+1)$-electron system in the sum over Φ_j. The selection must achieve consistency between the first and second sums in Eq. (10). Various selection methods affect the energies of bound states of configuration $2s^22p^6np\ ^2P^o$. The autoionizing resonances in the photoionization cross sections would be similarly affected. For the simpler case of inner-shell photoionization of beryllium one could carry out the selection of the necessary bound-state configurations manually [24]. For the case of sodium more than 1500 configurations are involved. Automatic selection procedures for the bound-state configurations that used Racah algebra and fractional parentage techniques were introduced into two earlier versions of the R-matrix codes by Berrington *et al.* [21,41]. However, these codes do not carry out this particular selection process correctly. An elaborate piece of coding was the key development that made inner-shell photoionization calculations that achieved a high degree of accuracy. This code is still unpublished.

2. The numerical solution

The number N_F of ''free'' channels and N_B of bound states included in the CC expansion as given by the two sums of Eq. (10) were 35 and 626 for $^2S^e$ and 65 and 1586 for the $^2P^o$ states, respectively, when the first 39 target states listed in Table III were included. The free wave functions had to extend over an energy range of 10 Ry, which in turn required a large number of basis states (39). We used for the internal region an R-matrix radius $a=29.2a_0$, automatically computed from the requirement that the radial functions had to have decayed to relative magnitude 10^{-3} at the boundary. We included all channels with scattered electron angular momenta $l\leqslant 3$. In the asymptotic region the solutions F had to be obtained at a sufficiently fine energy mesh so as to delineate the resonance structures. Immediately below threshold results were averaged over the resonances converging on that threshold using a method [41] originally formulated by Gailitis.

3. Consistency checks

With such an elaborate close-coupling expansion it was necessary to test the setup rigorously. The agreement between calculated bound-state energies and experimental values provides a good test for the accuracy of the mathematical model and for the consistency of the CC expansion in Eq. (10). For photoionization from the ground state wave functions are required only for the lowest bound state of the ^2S series and for three states of the $^2P^o$ series. The latter differ only formally from bound states by their asymptotic behavior. Our calculated effective quantum numbers for the lowest members of the $1s^22s^22p^6ns(^2S^e)$ and $-np(^2P^o)$ Rydberg series compare well with experimental determinations [29]. Similarly, our calculated ionization potentials (Table II) for the first and second subshell ionization thresholds are in excellent agreement with experiment.

We used three different methods for selecting the $(N+1)$-electron configurations in the second sum of Eq. (10), i.e., (i) omit all $(N+1)$-electron configurations that include any correlation orbital $\bar{5}l$, (ii) omit all configurations that include two correlation orbitals $\bar{5}l$ and $\bar{5}l'$, and (iii) include correlation configurations with two nonspectroscopic orbitals $\bar{5}l$ and $\bar{5}l'$ up to $\bar{5}l^2$. Only the third method gives results that match the experiment for the energies and effective quantum numbers of the terms of the $1s^22s^22p^6np\ ^2P^o$ Rydberg series. This last choice is the only correct choice since, during the optimization procedure in the CIV3 code, we used different combinations of $\bar{5}l$ orbitals in order to improve the ground state of Na^+. Therefore, we have to account for this also in the $(N+1)$-electron system, even though these configurations are not spectroscopic configurations. Such good agreement with experiment for the bound-state energies for the series $1s^22s^22p^6np\ ^2P^o$ is a necessary condition for predicting satisfactorily the energies of the autoionizing resonances $1s^22s2p^63snp(^2P^o)$ converging to the thresholds for ejection of a $2s$ electron because we used the same CI and CC expansions for both. Good agreement with experiment is also obtained for these quasibound states, although they have inner-shell vacancies and excited outer electrons and thus are very difficult to obtain in any *ab initio* calculation.

The present theoretical setup can equally well produce oscillator strengths for neutral sodium as photoionization cross sections. The consistency of the close-coupling expansion as given by the two sums in Eq. (10) has been checked by calculating the oscillator strengths in the length and velocity formulations and by comparing them with previously determined experimental and theoretical data. Our results agree well with other compilations: RPAE results by Amusia and Cherepkov [12], multiconfiguration Hartree-Fock results by Froese-Fischer [42], Hartree-Fock results by Biemont [43], and close-coupling results using polarized pseudostates by Butler and Mendoza [44]. The close agreement between our results obtained in the length and velocity formulations is satisfactory throughout, *which is no mean achievement* considering the extent of the present CC expansion. The differences arise from inconsistencies in the two sums of Eq. (10) and, especially for weak processes, from loss of numerical accuracy due to cancellation effects. In *ab initio* close-coupling and R-matrix calculations, the length form gives the most reliable results because the velocity form depends more on the potential in the inner region that is less well known than that in the outer region. As a result of these checks, there is no obvious shortcoming in the target representation or the CC expansion, so they should form a sound basis for photoionization calculations.

4. Angular distribution parameter

The relation between the asymmetry parameter β and the differential cross section $d\sigma(L_iS_i \rightarrow L_fS_f)/d\Omega$ to the integrated cross section σ_{tot} has been given in Eq. (1). In contrast to the integrated cross section, the angular anisotropy parameter depends on the total phase difference. A comparison of calculated β parameters with experiment is a sensitive test for the accuracy of the atomic potential. To calculate the parameter, one has to sum over products of transition amplitudes multiplied by algebraic coefficients. For better physical insight we write the expression in terms of the transferred angular momentum l_t defined as [45,46]

$$\vec{l}_t = \vec{L}_f - \vec{L}_i = \vec{1} - \vec{l}_f ,$$

where

$$Na(\vec{L}_i) + h\nu = Na(\vec{L}_f) + e^-(\vec{l}_f),$$

$$\vec{L} = \vec{L}_f + \vec{l}_f = \vec{L}_i + \vec{1}.$$

We obtain for β_{if}

$$\beta(L_iS_i \rightarrow L_fS_f)$$

$$= \frac{8\pi^2 \alpha a_0^2 C}{\sigma(2L_i+1)} \sum_{l_f, l_{f'}} \exp\left[-i(\sigma_{l_f} - \sigma_{l_{f'}}) + \frac{i\pi}{2}(l_f - l_{f'}) \right]$$

$$\times ([l_f][l_{f'}])^{1/2} \langle l_f 0 l_{f'} 0 | 20 \rangle \langle 1010 | 20 \rangle$$

$$\times \sum_{l_t} (-1)^{l_t} (2l_t+1) W(1 l_f 1 l_{f'} ; l_t 2) T^{L_t}_{L_i 1, L_f L_{f'}})^*, \quad (11)$$

with the notation $[l] = (2l+1)$, where

$$T^{l_t}_{L_i 1, L_t l_f} = \sum_L (-1)^L [L]^{1/2}$$

$$\times \begin{Bmatrix} 1 & L_i & L \\ L_f & l_f & l_t \end{Bmatrix} \langle \Psi_i \| M \| \Psi_f^- \rangle .$$

$C = \omega$ or ω^{-1} and $M = \Sigma_{j=1}^{N+1} r_j$ or $\Sigma_{j=1}^{N+1} \partial/\partial r_j$ in the length and velocity formulations, respectively. The usual notation for the Clebsch-Gordan coefficients and 6-j symbols applies and the σ_l in the exponential are the Coulomb phases. Individual cross sections $\sigma(L_iS_i \rightarrow L_fS_f)$ are not observed because of limited experimental resolution. For comparison with experiment, we have to use a weighted average as given in Sec. IV B.

IV. RESULTS

Before presenting our experimental and theoretical results for the relative values of the partial subshell photoionization cross sections and the asymmetry parameter β, we would like to emphasize that the ultimate test of theory by experiment is indeed the comparison of the absolute values of all partial subshell photoionization cross sections. Comparing experimental and theoretical values for a total subshell cross section is also of interest. The results of this comparison should, however, be taken with great caution because there might be some unexpected cancellations in the theoretical calculations. From the experimental point of view, measuring relative partial cross sections, i.e., branching ratios, provides the most accurate quantities that can be obtained by electron spectrometry. For atomic sodium, a comparison of the absolute values of cross sections experimentally determined and theoretically calculated cannot be made with an uncertainty better than 25–30%. Only in the rare gases where the total photoabsorption cross section has been measured within 2–3% can such a comparison be made to a similar uncertainty.

We will present our results in the following way. Although we have not made new measurements of the total photoabsorption cross section, we will first discuss the present status of the experimental and theoretical data for this cross section. Then we will present the relative values of the partial cross sections, normalizing the experimental values to single $2p$ photoionization and comparing them with the theoretical data obtained from the ratio of the calculated partial cross sections. Finally, the absolute values of each partial cross section resulting experimentally from the partition and normalization procedures will be compared with the theoretical results resulting directly from the calculations. Taking into account the uncertainty of 25% in the photoabsorption data, this last comparison alone will not allow us to distinguish several correlated calculations. Only by considering both relative and absolute partial cross sections we will be able to draw some conclusion about the validity of the various theories. Finally, the values of the β parameter, measured for the main line and for two classes of satellites, will be presented and discussed.

In the following figures, the data shown for the branching ratios are the experimentally measured values. For the absolute values of the partial cross sections, the experimental data are the results of a fitting procedure smoothly averaging in

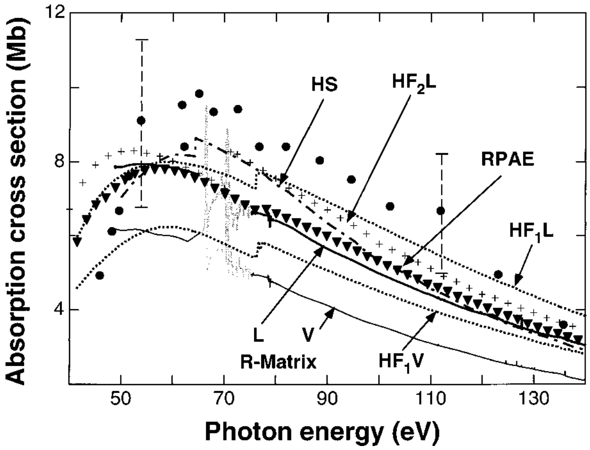

FIG. 6. Total photoabsorption cross section of atomic sodium. Experimental results: closed circles, from Ref. [2]. Theoretical results: present R-matrix calculations, full lines (length and velocity forms); RPAE results, closed triangles; HF$_1$ results, dotted lines, from Ref. [13]; HS results, dash-dotted line; HF$_2$ results, crosses, from Ref. [14]. The error bar for the experimental values is shown only at two photon energies.

the continuum range through all measured values of the branching ratios. They are shown as closed circles. The error bar resulting from the partition procedure (in general 5% or a little less) is indicated for every data point in the figures. The overall resulting error including the uncertainty on the measurements of the total photoabsorption cross section (20–25%) is shown as dashed vertical bars, at only one or two photon energies for better clarity. The resulting uncertainty of the absolute values of the partial cross sections is typically 25–30%.

In addition to our theoretical results obtained using both length (L) and velocity (V) formulations, we show also, in the resonant energy range below the $2s$ ionization threshold, the curves (labeled L-C) resulting from the convolution of our L results with the spectral resolution. They differ from the *ab initio* calculations because the finite experimental resolution decreases the value of the cross sections at the resonance energy and broadens the resonance structure. In order to achieve a better comparison with the experiment on a relative scale, our L-C curves have been also normalized to the measured experimental cross sections in the continuum region. In the figures presenting the variation of the cross sections over the whole energy range, the resonant structures are shown as gray curves only, the other figures showing in detail the resonant energy behavior.

A. Photoionization cross sections

1. The total photoabsorption cross section

Measurements of the photoabsorption spectrum of Na in the vacuum ultraviolet region were performed by Wolff *et al.* [6] on a relative scale. The measured spectrum was adjusted to be close to the cross section calculated by McGuire [10] using a one-electron model and the Herman-Skillman potential [47]. Later on, Codling, Hamley, and West [2] measured the absolute cross section. They estimated their averaged error to be 20–25%. In Fig. 6 we show the results of Codling, Hamley, and West together with those of the theoretical calculations. Our theoretical values of the photoabsorption cross section (R matrix, L, and V) are the sum of all partial cross sections that would leave the ion in any of the 39 target states of Na$^+$ that are energetically accessible (see the list in Table II). The double photoionization cross section has not been calculated in the present work, but it is known to be only about 1% of the total cross section [48,49]. Earlier calculations shown also in Fig. 6 are the HS results [14], two series of Hartree-Fock calculations (HF1 [13] and HF2 [14]), and the RPAE [11–13]. We selected only the results introducing the theoretical values of the $2s$ ionization thresholds in the calculations. For the HS and HF$_2$ results (only the length form of the HF$_2$ calculation is shown here for comparison with the HF$_1$ results), the total $2p$ and $2s$ cross sections have been both calculated; the curves shown in the figure are the total $2p$ cross section below and the sum of $2p+2s$ total cross sections above the $2s$ ionization thresholds, respectively. The RPAE, HF$_1$$L$ and HL$_1$$V$ curves show the sum of the total $2p+3s$ cross sections (the $3s$ and the $2s$ photoionization cross section are less than 1% and 10% of the $2p$ cross section in this energy range, respectively).

One observation is that most of the theoretically calculated values of the $2s$ ionization thresholds ($^{1,3}S$) are in great disagreement with the experimental values of 70.9 and 71.3 eV for $2s2p^63s$ $^3S^e$ and $^1S^e$, respectively. Only the results of our R-matrix calculations (70.97 and 71.38 eV, respectively) are in excellent agreement with experiment. Also evident is that the highly correlated calculations (RPAE) [11–13] performed more than 20 years ago and the most recent ones, our R-matrix L calculations, are in good agreement with each other, even when one considers that the RPAE results do not include the total $2s$ cross section (we will see later that the $2s$ to $2p$ branching ratio is close to 10% over the energy range involved here). A third observation is that the large experimental uncertainty does not allow us to discriminate between most of the theoretical calculations of the total cross section. Over most of the photon energy range, almost all theoretical results, within two exceptions (the HF$_1$$V$ and our V calculations), lie within the error bars of the experimental measurements. Interestingly enough, the simplest HS calculations give agreement with experiment that is apparently as good as that of the highly correlated RPAE calculations. This means that either correlations have a weak effect for the $2p$ subshell of sodium or, and most likely when one considers the large relative intensity of the correlation satellites, neglecting correlations introduces an artificial agreement with experiment because of cancellations. This conclusion confirms our earlier statement that a meaningful comparison of theory with experiment requires also measurements and calculations of the partial subshell cross sections.

In the 64–72 eV photon energy range, shown over an extended scale in Fig. 7, one finds Rydberg series of resonances due to excited states with a $2s$ vacancy. Numerical values of the resonant energies and associated quantum numbers are given in Table IV. These resonances are differentially analyzed in the partial cross sections for ionization plus excitation, but one is concerned here with their overall effect. The series due to parent configuration $1s^22s2p^63s$ ^3S is by far the strongest. The enhancement is entirely due to constructive interference of the two Rydberg series $2s2p^63s(^3S)np$ and $2s2p^63s(^1S)n'p$ with resonances pil-

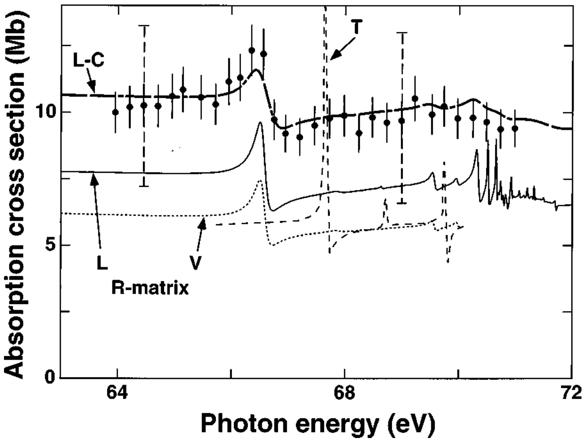

FIG. 7. Total photoabsorption cross section of atomic sodium in the resonance region. Present theoretical R-matrix results, full line (length form) and dotted line (velocity form); calculations by Tayal *et al.*, dashed line (length form) from Ref. [20]; present experimental results, closed circles. The small error bars results from the error introduced by the addition of the partial cross sections. The total error, including the error due to the photoabsorption measurements of Ref. [2], is indicated at two photon energies as vertical dashed lines. The L-C curve results from convolution of our *ab initio* L results with the spectral resolution; it is also normalized to the experimental value of the single $2p$ cross section in the continuum energy region (near 64 eV).

ing up as the ^3S threshold is reached at 70.97. Beyond that threshold, one sees the smaller resonances of the $(^1S)n'p$ series that converge on the ^1S threshold at 71.38 eV. Comparing with experiment, one finds that the resonance structure near 66 eV is well reproduced by the present calculations. The calculations by Tayal, Msezane, and Manson [20] show the structure shifted to higher energies. Our calculated (length form) and measured values disagree by 15% in magnitude around the broad maximum. Earlier calculations [17] agree in this respect with our results, but the calculated cross section (length form) by Tayal, Msezane, and Manson [20] reaches only two-thirds of the measured magnitude. The onset of the photoionization of the $2s$ electron at the $1s^22s2p^63s$ ^3S and ^1S thresholds is masked by resonances.

TABLE IV. Rydberg series of resonances $2s^22p^63s$ $^2S \rightarrow 2s2p^63snl$ $^2P^o$ and the associated effective quantum numbers.

Parent term	nl	Calc.	Obs.[a]	Obs.[b]	Obs.[c]	n^* (Calc.)
$2s2p^63s(^3S)$	$3p$	66.46	66.37	66.6	66.5	1.713
$2s2p^63s(^3S)$	$4p$	69.5	69.4	69.6		2.866
$2s2p^63s(^3S)$	$5p$	70.25				4.023
$2s2p^63s(^3S)$	$6p$	70.52				5.045
$2s2p^63s(^1S)$	$3p$	67.8	67.8	68.		1.882
$2s2p^63s(^1S)$	$4p$	69.9				2.780
$2s2p^63s(^1S)$	$5p$	70.8				3.817
$2s2p^63s(^1S)$	$6p$	71.1				4.845
$2s2p^63p(^3P^o)$	$4s$	72.9	72.7			2.318
$2s2p^63p(^1P^o)$	$4s$	73.5	73.3			2.559

[a] Reference [50].
[b] Reference [6].
[c] Present work.

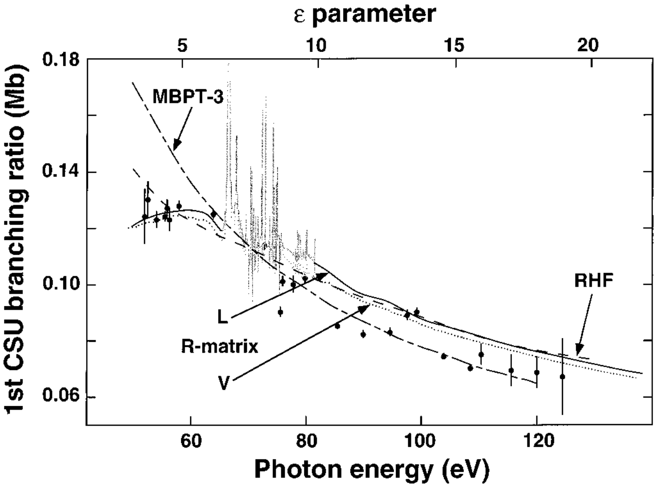

FIG. 8. Branching ratio $2p^53p$ to $2p^53s$ for the first CSU satellite following $2p$ photoionization in sodium. Theoretical results are the present R-matrix calculations in the length (L, full line) and velocity (V, dotted line) forms, the RHF calculations [18] (dashed line), and the MBPT-3 calculations [22] (dash-dotted line). The experimental results are partly from Ref. [8] (large error bars) and partly from this work (small error bars).

Only calculations such as those by McGuire [10] that do not include coupling between lower channels and those for ionization of the $2s$ electron obtain a marked step at this threshold.

We have also calculated the resonant structure of the photoabsorption cross section near the two $2p$ ionization thresholds $1s^22s^22p^53s$ ^3P and ^1P at 38.04 and 38.46 eV, respectively. Our R-matrix results for the energy position of 16 members of the $2s^22p^63s \rightarrow 2s^22p^53s(^{1,3}P^o)nl$ Rydberg series agree very well with the experimentally measured photoabsorption spectrum [6,50,51].

2. Branching ratios and relative cross sections

Figures 8 and 9 present experimental and theoretical values of the branching ratios for CSU and SU correlation satellites following $2p$ subshell photoionization over the photon energy extending from 50 to 140 eV. The results over the resonant energy region are shown in more detail in Figs. 10–12.

The branching ratio for the first CSU satellite, i.e., the ratio between the intensity of peaks 2 and 1 in Fig. 3 ($2s^22p^63s+h\nu \rightarrow 2s^22p^53p+e^-$ to $2s^22p^63s+h\nu \rightarrow 2s^22p^53s+e^-$), is shown in Fig. 8 in the continuum energy region. The experimental results with the smallest error bars are the most recent ones. In addition to our experimental and theoretical results, two other sets of theoretical results can be seen in Fig. 9: the RHF results [18], using relaxed wave functions for the ionic state, and the results of the MBPT-3 calculations [22]. In this figure as well as in Fig. 10, the top scale represents the values of the reduced ε parameter, where ε is defined [4] as the ratio between the excess energy of the shake electron and the additional energy necessary to produce the satellite state. The CSU experimental branching ratio decreases slowly with increasing photon energy, from about 12% at 60 eV to about 7% at 130 eV. This behavior reflects the mechanism of production of these

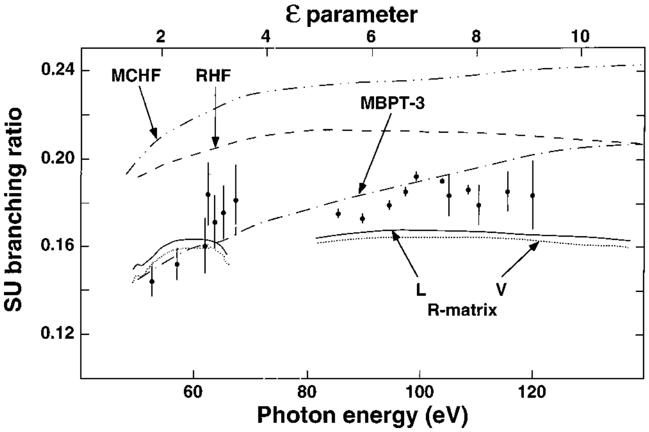

FIG. 9. Branching ratio $2p^5(4s+3d)$ to $2p^53s$ for the first SU satellite following $2p$ photoionization in sodium. Theoretical results are the present R-matrix calculations in the length (L, full line) and velocity (V, dotted line) forms, the RHF calculations [18] (dashed line), the MBPT-3 calculations [22] (dash-dotted line), and the MCHF calculations [23] (dash–double-dotted line). The experimental results are partly from Ref. [7] (large error bars) and partly from this work (small error bars).

satellites (mainly inelastic scattering of the outgoing $2p$ photoelectron by the polarized ionic core). The experimental value of the branching ratio has not yet reached a constant limit for values of ε close to 20. The RHF results are shown here as calculated in the L form (the V results are close to them). They are a little high at all photon energies. Our R-matrix results present the same behavior, but are the only ones showing a small maximum at about 80 eV. The MBPT-3 results are in excellent agreement with the experimental data over most of the photon energy range. They deviate only below 60 eV.

Presented in Fig. 9 is the branching ratio for the first SU satellite, including the unresolved $2p^53d$, i.e., the ratio between the intensity of peaks 3 and 1 in Fig. 3 [$2s^22p^63s+h\nu\rightarrow 2s^22p^54s$ (and $3d$) $+e^-$ to $2s^22p^63s+h\nu\rightarrow 2s^22p^53s+e^-$]. Here the branching ratio increases slowly with increasing photon energy and reaches a plateau value for values of the ε parameter higher than 5, i.e., much sooner than in the case of the CSU satellite. Such a behavior is expected in the sudden approximation theory [52] for the intensity of the $2p^54s$ shake-up satellites. The small increase in the experimental values near 100 eV is due to the existence of doubly excited $2p^4nln'l'$ resonances that are not introduced in the theoretical model. The details of our R-matrix calculations show that the overall predicted intensity of the transitions to all $2p^53d$ satellite states is about

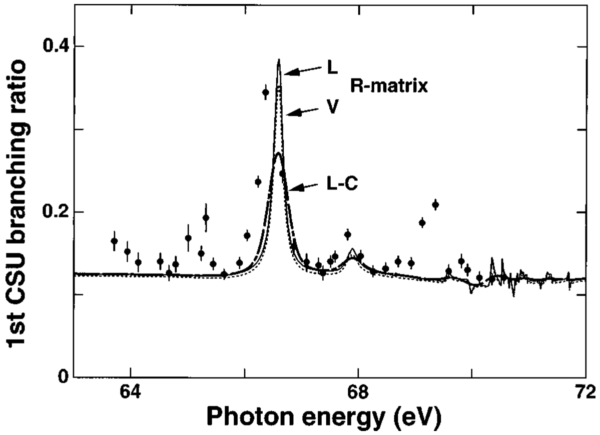

FIG. 10. Branching ratio $2p^53p$ to $2p^53s$ for the first CSU satellite in the resonance region. Theoretical results are the present R-matrix calculations in the length (L, full line) and velocity (V, dotted line) forms. The experimental results are partly from Ref. [8]. In this figure as well as in Figs. 11 and 12, the L-C curve results from convolution of our *ab initio* L results with the spectral resolution; it is also normalized to the experimental value of the single $2p$ cross section in the continuum energy region (at 64 eV).

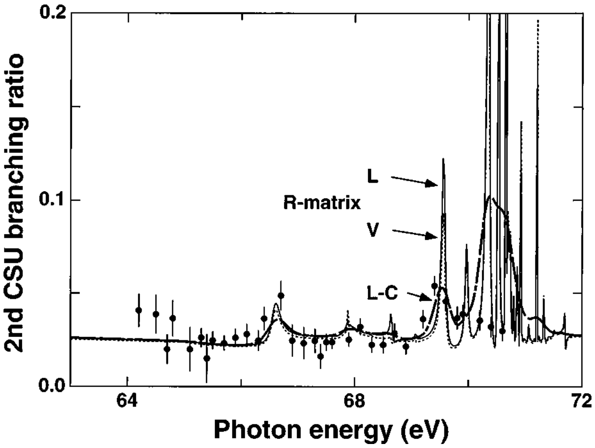

FIG. 11. Branching ratio $2p^54p$ to $2p^53s$ for the second CSU satellite of sodium in the resonance region. Theoretical results are the present R-matrix calculations in the length (L, full line) and velocity (V, dotted line) forms. The experimental results are from Ref. [13]. The L-C curve results from convolution of our *ab initio* L results with the spectral resolution and normalization to the experimental value of the single $2p$ cross section in the continuum energy region (at 64 eV).

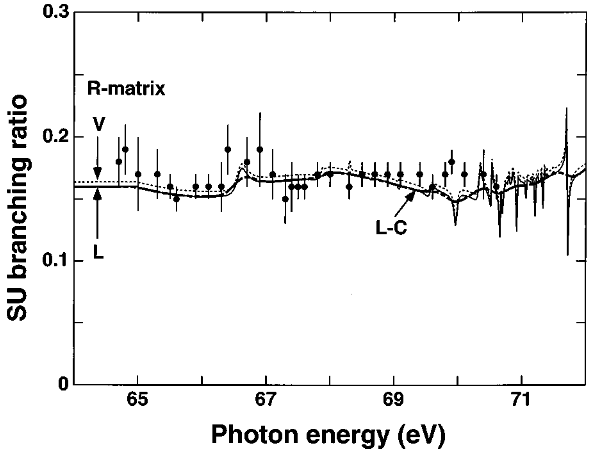

FIG. 12. Branching ratio $2p^5(4s,3d)$ to $2p^53s$ for the first SU satellite of sodium in the resonance region. Theoretical results are the present R-matrix calculations in the length (L, full line) and velocity (V, dotted line) forms. The experimental results are from Ref. [8]. The L-C curve results from convolution of our *ab initio* L results with the spectral resolution and normalization to the experimental value of the single $2p$ cross section in the continuum energy region (at 64 eV).

50% of the intensity of the transitions to the $2p^5 4s$ shake-up states. The results shown in Fig. 9 suggest that the energy dependence of the relative intensity for the $2p^5 3d$ satellites has the same behavior as for the main line and shake-up satellites, even though they cannot be explained by the sudden approximation. Our R-matrix and the MBPT-3 [22] results reproduce well the experimental behavior, while the RHF calculations [18] give higher values. The recent MCHF calculation [23] produces results that are even higher, by 30–40 %.

The branching ratios for the first ($2p^5 3p$ ionic states) and the second ($2p^5 4p$ ionic states) series of CSU satellites vary rapidly in the vicinity of the first $2s \rightarrow 3p$ resonances, as it can be seen in Figs. 10 and 11, but not for the SU satellites presented in Fig. 12. Until recently, only our R-matrix results could be used for a meaningful comparison with experiment [13]. We have already seen that our energy calculations give results that are in excellent agreement with experiment, whereas the resonance energies calculated by other authors are in poor agreement with the experimental data. The significant differences between our experimental and theoretical values at the resonances is due to the fact that the spectral resolution is considerably larger than the natural width of the autoionizing resonances. This difference lowers the experimental values at resonance. Otherwise, our calculations give results in excellent agreement with the experimental data. They reproduce well the position of the first maximum in both first and second CSU satellite channels (Figs. 10 and 11) that are due to the $2s2p^6 3s(^3S)3p$ and $(^1S)3p$ resonances at 66.46 and 67.8 eV, respectively, as it can be seen in Table IV, where theoretical and experimental energy values are compared. The increase of the branching ratio at these resonances shows the importance of the CSU process (effect of selective autoionization). One can note the good agreement between our L and V results obtained for all branching ratios. Theoretical results obtained using the many-body perturbation theory [53] also show good agreement with the experimental data. A second maximum is experimentally observed at 69.5 eV in all channels. It is relatively strong in the second CSU satellite channel (Fig. 11). It is due to the $2s2p^6 3s(^3S)4p\ ^4P^o$ excited state. This resonance could be easily identified in the calculations, but there it is a relatively small feature in the experimental measurements for the instrumental reasons previously explained. The maximum observed at 65.2 eV (Fig. 10) is due to the excited state $2s2p^6 3s(^3S)3p\ ^4P^o$. Transitions to these quartet symmetry states are forbidden in LS coupling and are not obtained by the present calculation. In the SU satellite channel, the branching ratio remains fairly flat, as it should be, except for weak structures near the $(^3S)3p$ and $(^1S)3p$ resonances and for the quartet state resonance near 65 eV.

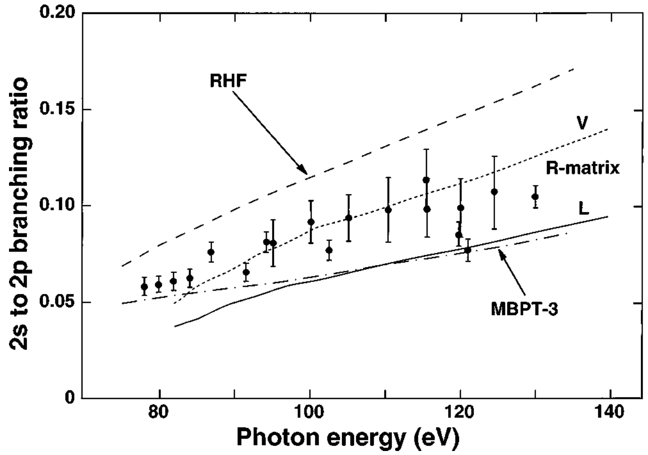

FIG. 13. Branching ratio $2s2p^6 3s$ to $2s^2 2p^5 3s$ following $2s$ and $2p$ photoionization in sodium. Theoretical results are the present R-matrix calculations in the length (L, full line) and velocity (V, dotted line) forms, the RHF calculations [18] (dashed line), and the MBPT-3 calculations [22] (dash-dotted line). The experimental results are from this work.

Figure 13 shows the branching ratio for photoionization of the $2s$ electron (the process $2s^2 2p^6 3s + h\nu \rightarrow 2s2p^6 3s + e^-$). Our experimental and theoretical results and a number of other theoretical results are shown. The experimental value of the branching ratio increases slowly with increasing photon energy. The RHF results [18] are definitely too high, whereas the MBPT-3 results [22] agree rather well with the experimental data. Our V results are generally in excellent agreement with the experimental observations. This is the only case where they are above the L results. This convergence of our experimental and theoretical results is quite satisfactory. Below 80 eV photon energy, one observes the effect of several resonances corresponding to double excitations of the $2s$ and $3s$ electrons. In particular, resonances are observed at about 73 and 77 eV, which can be attributed to the existence of the neutral $2s2p^6 3p4s$ and $2s2p^6 4s4p$ excited states [15]. Experimentally, we did not explore this resonant energy region in detail. In fact, the influence of these resonances on the $2s$ to $2p$ branching ratio is predicted to be relatively small and it would have been difficult to observe experimentally any effect because of the large instrumental window and small counting rates.

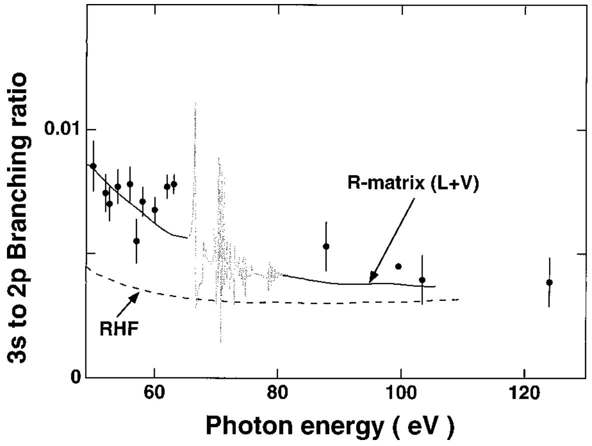

FIG. 14. Branching ratio $2s^2 2p^6$ to $2s^2 2p^5 3s$ following $3s$ and $2p$ photoionization in sodium. Theoretical results: our L and V R-matrix results are identical and are shown as the full line and the RHF results from Ref. [18] are shown as the dashed line. Experimental results (closed circles) are from this work.

Finally, we show in Fig. 14 the branching ratio for photoionization of a $3s$ electron. (the process $2s^2 2p^6 3s + h\nu \rightarrow 2s^2 2p^6 + e^-$). The value of the $3s$ to $2p$ branching ratio is lower than 1% and decreases with increasing photon energy. Our theoretical results (only the mean value of our L and V results is shown, both results being very close to each other)

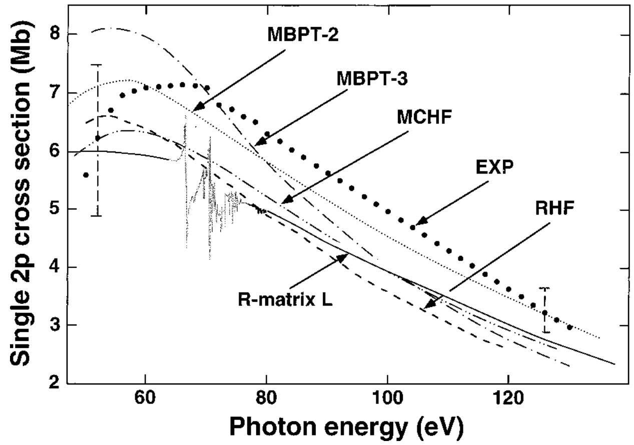

FIG. 15. Partial cross sections for single $2p$ photoionization of sodium leaving the ion in any one state of the configuration $1s^2 2s^2 2p^5 3s$. Theoretical results are the present R-matrix calculations in the length (L, full line) form, the RHF calculations [18] (dashed line), the MBPT-2 calculations [17] (dotted line), the MBPT-3 calculations [22] (dash-dotted line), and the MCHF calculations [23] (dash–double-dotted line). The experimental results (closed circles) are from this work. The total error, including the error due to the photoabsorption measurements of Ref. [2], is indicated at two photon energies as vertical dashed lines.

are the only ones to reproduce correctly the experimentally observed behavior. The RHF results [18] are too low by a factor 2 at low photon energy and agree with our experimental results only at the high-energy side of the photon range.

Because of a lack of resolution and beam time, we did not study in detail the $2p^4 nln'l'$ satellites. We estimated their relative intensity at a few photon energies and found it to be on the order of 2% of the $2p$ single photoionization, which is similar to the values measured in neon [4,5]. The fact that these satellites have about the same relative intensity in neon and in sodium confirms that the existence of the $3s$ electron has little influence on the $2p$ subshell photoionization processes. In other words, correlation effects other than core relaxation are very weak between the outer and the first inner subshell. The relatively high intensity of the $2p^5 nl$ satellites is mainly due to core relaxation and inelastic scattering, i.e., to final-state interactions in the core-ionized Na^+ ion, and also to the high oscillator strength of the optical $3s \rightarrow 3p$ transition.

3. Absolute values of the partial cross sections

In Figs. 15–20 the absolute values of the partial photoionization cross sections are presented. Figures 15–17 show the variation of the single $2p$ cross section (ML) and the cross sections for $2p$ photoionization with simultaneous excitation to the $2s^2 2p^5 3p$ ionic states (first CSU) and to the $2s^2 2p^5 (4s+3d)$ ionic states (mainly the first SU satellite), over the whole photon energy range, respectively. For better reading, the cross sections in the resonant energy region between 64 and 72 eV are represented in full detail in Figs. 18–20, respectively. The theoretical results are presented as the sums over partial cross sections that leave the ion in any one state of configuration $1s^2 2s^2 2p^5 nl$ since the present photoelectron experiments cannot resolve the fine structure of the final ionic states. For direct photoionization cross sections into the continua (Figs. 15–17), only the L results of all theoretical calculations are shown for comparison with experiment.

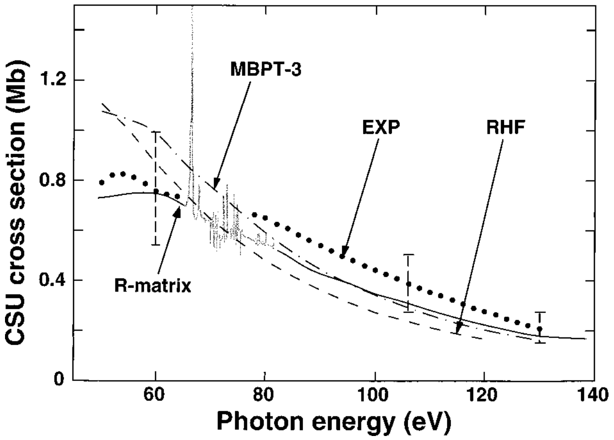

FIG. 16. Partial cross section for photoionization of sodium leaving the ion in any one state of the configuration $1s^2 2s^2 2p^5 3p$. Theoretical results presented in the length form are the present R-matrix calculations (L, full line), the RHF calculations [18] (dashed line), and the MBPT-3 calculations [22] (dash-dotted line). The experimental results (closed circles) are from this work. The total error, including the error due to the photoabsorption measurements of Ref. [2], is indicated at three photon energies as vertical dashed lines.

Five theoretical calculations are available for the single $2p$ cross section seen in Fig. 15. The RHF [18] and MCHF [23] calculations agree rather well with ours. At low photon energy, the RHF [5], the MCHF [10], and one of the three many-body perturbation theories (MBPT-2 [17]) calculations are all in agreement with our experimental data, as well as our L R-matrix results. The V form of our calculations is significantly lower by about 20%. At high photon energy,

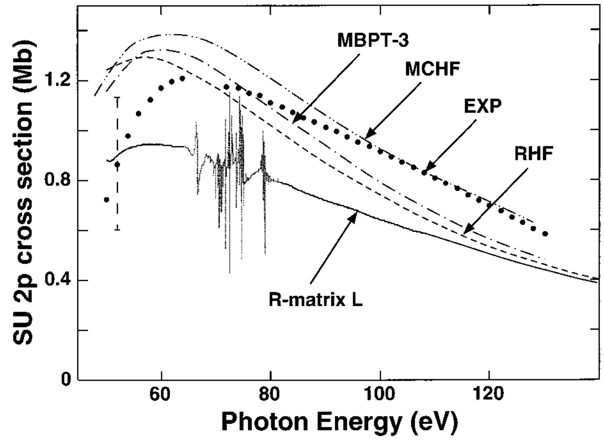

FIG. 17. Partial cross sections for photoionization of sodium leaving the ion in any one state of the $2s^2 2p^5 4s$ and $2s^2 2p^5 3d$ configurations. Theoretical results are, in the length form, the present R-matrix calculations (L, full line), the RHF calculations [18] (dashed line), the MBPT-3 calculations [22] (dash-dotted line), and the MCHF calculations [23] (dash–double-dotted line). The experimental results (closed circles) are from this work. The total error, including the error due to the photoabsorption measurements of Ref. [2] is indicated at one photon energy as a vertical dashed line.

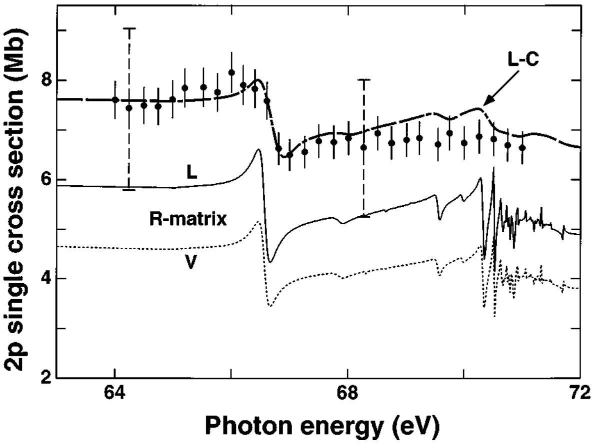

FIG. 18. Partial cross section for single photoionization of sodium leaving the ion in any one state of the configuration $1s^22s^22p^53s$ in the resonant region. Theoretical results are the present R-matrix calculations in the length (L, full line) and velocity (V, thin dotted line) forms. The experimental results (closed circles) are from this work. They have been obtained by measuring the variation of the ML signal over the resonance region. The small error bars include only the errors introduced by the partition of the total cross section. The total error including the error in the photoabsorption measurements is shown at two photon energies as a vertical dashed line. The L-C curve results from convolution of our *ab initio L* results with the spectral resolution; it is also normalized to the experimental value of the single $2p$ cross section in the continuum energy region (at 64 eV).

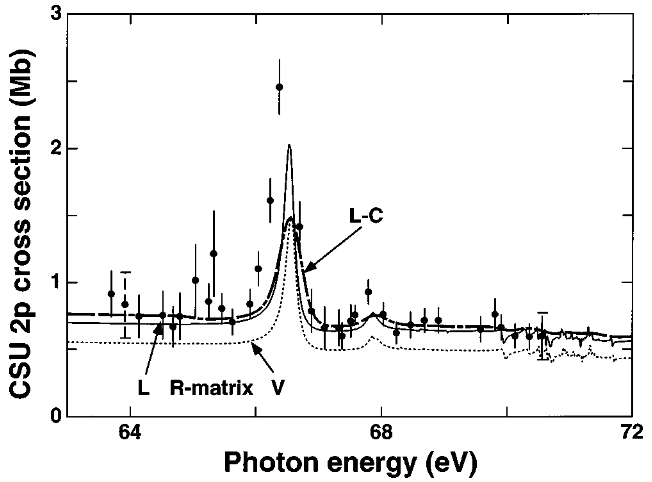

FIG. 19. Partial cross section for photoionization of sodium leaving the ion in any one state of the configuration $1s^22s^22p^53p$ in the resonant region. Theoretical results are the present R-matrix calculations in the length (L, full line) and velocity (V, thin dotted line) forms. The experimental results (closed circles) have been obtained by measuring the variation of the CSU satellite signal over the resonance region. The small error bars include only the error introduced by the partition of the total cross section. The total error including the error in the photoabsorption measurements is shown at two photon energies as a vertical dashed line. The L-C curve results from convolution of our *ab initio L* results with the spectral resolution; it is also normalized to the experimental value of the single $2p$ cross section in the continuum energy region (at 64 eV).

most of the calculations, including ours, provide cross-section values that are lower than the experiment. Only the MBPT-2 results [22] stay in good agreement with experiment over the whole photon energy range. However, all calculations lie within the experimental error bars, but the figure indicates that there are still unsolved differences between theory and experiment for the single $2p$ photoionization cross section.

The conclusions are a little different for the first CSU cross section shown in Fig. 16. At low photon energy, the only theoretical results in agreement with the experimental data are our L R-matrix calculations. Above 80 eV photon energy, the RHF [18] and MBPT-3 [22] results are very close to ours and reproduce well the experimental energy dependence. The absolute values of the calculated cross sections are in agreement with the experimental data within the experimental error. For the first SU cross section, shown in Fig. 17, the experimental data present the same energy dependence as the single $2p$ cross section, as expected. Again, most calculations give results that are generally lower than the measured values, however, within the error bars. Our calculations include transitions to final states having both $2p^54s$ and $2p^53d$ electronic configurations since the instrumental resolution does not allow us to distinguish between the two corresponding photoelectron lines. Transitions to states with $2p^53d$ electronic configurations have not been taken into account in any other calculations. The situation is the same as for the single $2p$ cross section: The MBPT-3 [22], RHF [18], and MCHF [23] results are in good agreement with experiment, except below 60 eV, while our V R-matrix results are again lower than the experimental data. Our L results are also low, but within the 30% experimental uncertainty. The fact that both single $2p$ and first shake-up calculated cross sections seem to be a little too low explains that our calculated SU branching ratio is in good agreement with experiment. It is clear that the discrepancy between our R-matrix calculation and experiment is mainly due to a shortfall of the cross section for the main line.

The conclusions are similar for the single $2p$ cross section in the resonant energy region. In Fig. 18 (as in Figs. 19 and 20), the data have been obtained by scanning each photoelectron signal through the resonant region and by normalizing the data to the photoabsorption cross section at 64 eV. The density of atomic sodium in the source volume was checked at regular time intervals by measuring systematically the same photoelectron spectrum at a given photon energy (64 eV). For the variation of the $2p$ single cross section over the resonant energy region, our R-matrix and the MBPT [53] calculations are available for comparison with experiment. Again, the L results are barely in agreement with the experimental data, whereas the V results are significantly lower. Our L-C curve is in good agreement, on a relative scale, with our experimental results. The V form of the MBPT results, not shown in the figure, is in very good agreement with the experimental data.

The cross sections for photoionization to the first CSU ($2p^53p$ final-state configuration) and SU [$2p^5(4s+3d)$] satellites states are shown in Figs. 19 and 20, respectively. The general shapes of the experimental curves are well reproduced by our calculations, as it can be seen on our normalized curves L-C. The absolute values are again a little too low, although the L forms are always in agreement with

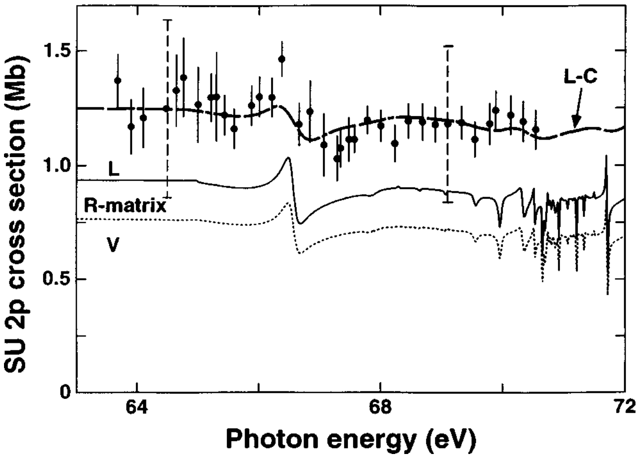

FIG. 20. Partial cross section for photoionization of sodium leaving the ion in any one state of the $1s^22s^22p^54s$ and $1s^22s^22p^53d$ configurations in the resonant region. Theoretical results are the present R-matrix calculations in the length (L, full line) and velocity (V, thin dotted line) forms. The experimental results (closed circles) have been obtained by measuring the variation of the satellite signal over the resonance region. The small error bars include only the error introduced by the partition of the total cross section. The total error including the error in the photoabsorption measurements is shown at two photon energies as a vertical dashed line. The L-C curve results from convolution of our *ab initio* L results with the spectral resolution; it is also normalized to the experimental value of the single $2p$ cross section in the continuum energy region (at 64 eV).

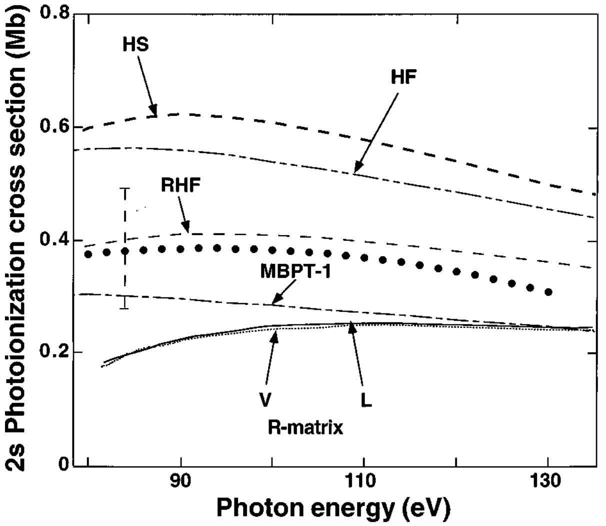

FIG. 21. Partial cross sections for single $2s$ photoionization of sodium leaving the ion in any one state of the configuration $1s^22s2p^63s$. Theoretical results are the present R-matrix calculations in the length (L, full line) and velocity (V, dotted line) forms, the RHF calculations [18] (thin dashed line), the MBPT-1 calculations [16] (dash-dotted line), the HS calculations (thick dashed line) and the HF calculations (dash–double-dotted line) calculations [14]. The experimental results (closed circles) are from this work. The total error, including the error due to the photoabsorption measurements of Ref. [2], is indicated at one photon energy as a vertical dashed line.

the experimental data when one takes into account the total uncertainty.

The variation of the single $2s$ photoionization cross section over the whole photon energy range is shown in Fig. 21. The energy dependence of this cross section is remarkably flat. Both theoretical MBPT-2 [17] and RHF [18] results are in good agreement with experiment. The theories that do not include any correlation effects, such as the HS and the HF calculations [13,14], do not agree with our experimental data. They predict too high values of the $2s$ cross section. This effect was predicted by the RPAE calculations [54], soon followed by the measurements [55], in the case of the $2s$ photoionization cross section of neon more than 20 years ago. It was also shown at this time that the results of Hartree-Slater [56] and Hartree-Fock [57] calculations for neon were 30% higher than the experimental values [4,53]. This was confirmed later by additional measurements [58]. The results of the R-matrix calculations [59] were still higher than the experimental data, suggesting that electron correlations were not fully accounted for. Here, in the case of sodium, our R-matrix results are too low, although the L and V forms are in excellent agreement with each other. This may be explained by the fact that ionic states with a $2s$ vacancy are at the high-energy end of our CC target representation (see Table III) and it may well be that some higher configurations should be explicitly included in the basis to fully describe the $2s$ cross section behavior.

Finally, we present in Fig. 22 the variation of the $3s$ photoionization cross section over the continuum energy region. This is a very small cross section and therefore prone to loss of numerical accuracy. Our R-matrix results are lower than our experimental data up to about 100 eV photon energy. The results of the RHF calculations [18] are even lower than ours at low photon energy, but join them at higher energies.

B. Asymmetry parameters

Like for the partial cross sections, the fine structure could not be experimentally resolved except at very low energies

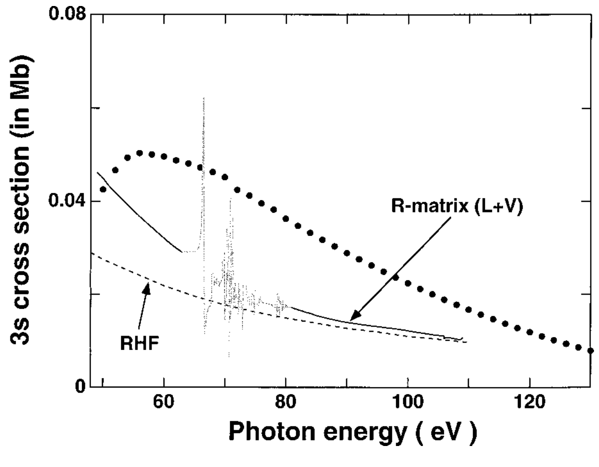

FIG. 22. $3s$ photoionization cross section in atomic sodium. Our length and velocity R-matrix results coincide and are shown as the full line; the RHF calculations [18] are shown as the dashed line. The experimental results (closed circles) are from this work. The total error, including the error due to the photoabsorption measurements of Ref. [2], is on the order of 30%.

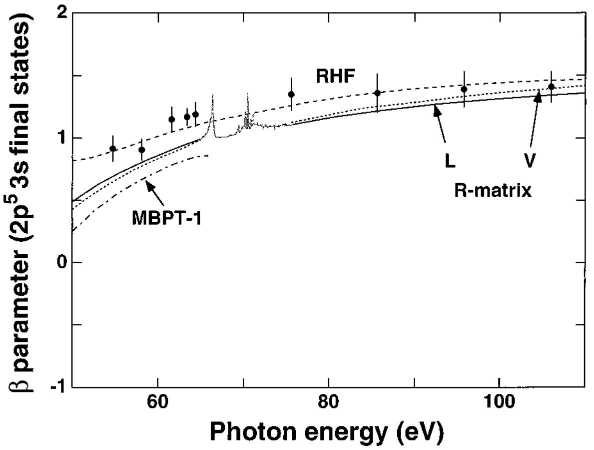

FIG. 23. Average asymmetry parameter for atomic sodium leaving the ion in the $2s^22p^53s$ states. Present theoretical results: length form (L, full line) and velocity form (V, dotted line); RHF calculations, L form (dashed line), from Ref. [18]; MBPT-1 calculations, L form (dash-dotted line), from Ref. [17]. Present experimental results, closed circles.

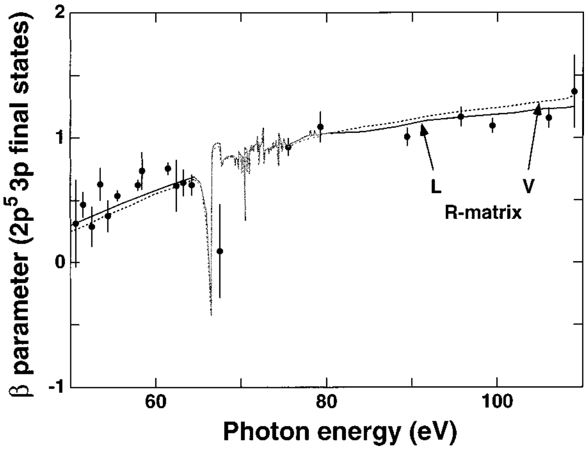

FIG. 24. Average asymmetry parameter for atomic sodium leaving the ion in the first CSU $2p^53p$ states. Present theoretical results: length form (L, full line) and velocity form (V, dotted line). Present experimental results, closed circles.

above the ionization threshold. Thus, for comparison, the individual theoretical results of the individual parameters had to be computed according to

$$\beta_{\text{average}}=\sum \beta_i\sigma_i \Big/ \sum \sigma_i . \qquad (12)$$

Our calculations and experimental results are compared in Figs. 23–25. The variation of the asymmetry parameter β for the photoelectrons ejected in single $2p$ photoionization is shown in Fig. 23. We note a rather strong energy dependence of β. There is a pronounced minimum (not shown in the figure) in all calculations around 40 eV photon energy, i.e., very near the $2p$ ionization thresholds. This low-kinetic-energy region could not be explored in our measurements because of the too-low transmission of the CMA. However, such a deep minimum has been theoretically predicted many years ago in the case of $2p$ photoelectrons of neon [54,57] and has been observed experimentally [60]. This phenomenon results from the interference of the phase shifts due to the Coulombic and the short-range potentials [61]. For sodium, the β parameter for the $2p$ main line has been calculated in a number of theoretical approximations: the HS and HF approximations by Theodosiou and Fielder [14], many-body perturbation theory (MBPT-1 by Chang and Kim [16], MBPT-2 by Isenberg *et al.* [17]), the RHF approximation by Craig and Larkins [18], and the MCHF approximation by Saha [23]. The HF results are a little lower than the RHF results and the two MBPT results are very close to each other. For clarity, we chose to show in Fig. 23, among the correlated calculations, only the RHF [18] and MBPT-1 [16] results (in the length form) to compare with our R-matrix calculations and our experimental data. Since the accuracy of the experimental values is independent of any normalization, the error bars are small (typically on the order of 5%) and the comparison of the calculated values with the experimental data is a valuable test of the various theoretical approximations. At first sight, the RHF results give apparently the best agreement with the experiment. Like for the absolute values of the partial cross sections, the highly correlated theories seem to produce results that are less in agreement with the measured values. This would imply that interchannel coupling effects are weak and might have been overestimated in the more sophisticated theories. However, one has to examine carefully which ionization threshold energies have been used in the calculations. The values used in the MBPT-1 [16] and RHF [18] calculations are in error by 1.5 eV and more than 3 eV, respectively, while the MBPT-2 calculations [17] used the experimental values. The R-matrix energy values are in extremely good agreement with the experimental data, like for the energies of the $2s$ resonances (see Table IV). These small differences, however, cannot be the main reason for the apparently better agreement of some of the theoretical values with experiment at *low* photon energy. It should be noted that for single $2p$ photoionization out of the $2p^53p$ excited sodium atom, the R-matrix values are in excellent agreement with the experimental data [62]. In the R-matrix calculations, the core polarization has been neglected. One can expect that this effect should be more important when the outer electron is in the $3s$ orbital than when it is in the $3p$ orbital because of the deeper penetration of the $3s$ orbital into the core region. Thus the better agreement of the R-matrix results with experiment for the excited sodium atom would mean that the core polarization effects are important and should not be neglected in the calculations. This point was already emphasized in the RPAE calculations of the total $2p$ subshell photoionization cross section [12].

Finally, we show in Figs. 24 and 25 the variation of the β parameter for photoelectrons corresponding to the first CSU and SU satellite channels, respectively. For the CSU channel, our R-matrix results are in good agreement with our experimental data. The most striking feature is the narrow minimum at the $2s2p^63s(^3S)3p\ ^2P^o$ resonance, seen in Fig. 24. The theoretically predicted behavior is qualitatively reproduced by the experiment. Our L and V forms are very close to each other. For the SU satellite channel (Fig. 25), one can draw the same conclusion as for the single $2p$ ionization channel, which is not surprising at first sight since the symmetry of the final states is the same in both cases. One should keep in mind, however, that the experimental results include

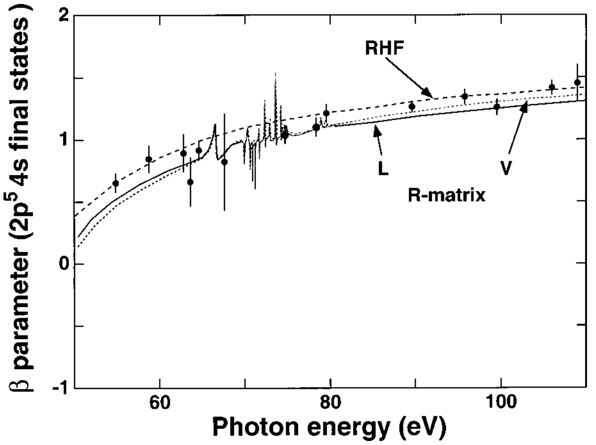

FIG. 25. Average asymmetry parameter for atomic sodium leaving the ion in the $2p^5(3d+4s)$ states. Present theoretical results: length form (L, full line) and velocity form (V, dotted line); RHF calculations (dashed line), from Ref. [18]. Present experimental results, closed circles.

also the angular dependence of the $2p^53d$ satellites and that our R-matrix calculations predict the $2p^53d$ to $2p^54s$ branching ratio to be on the order of 50%. The experimental accuracy does not allow us to discriminate between both groups of satellites; as for the branching ratio results (see Fig. 9), they could also show a similar energy dependence. The RHF results again give the best agreement with experiment.

V. CONCLUSIONS

This paper summarizes the results obtained during several years of experimentalists and theorists investigating together the photoionization processes in atomic sodium. The determination of branching ratios, i.e., of the partial cross sections on a relative scale, has been achieved over a photon energy range covering the inner-shell $2p$ and $2s$ resonant excitations as well as a wide continuum energy region above. Absolute values of the partial cross sections were also determined experimentally by normalizing the sum of the partial cross sections to the previously measured photoabsorption cross section. An inherent inaccuracy of 25% in these photoabsorption measurements is the main limitation in comparing theoretical and experimental values of the absolute cross sections. Nevertheless, the use of the photoelectron spectroscopy provided a full partition of a total photoabsorption cross section into its partial components for the sodium atom.

Theoretically, the comparison of the total $2p$ subshell cross section with the experiment does not allow us to discriminate between one-electron results and highly correlated calculations. Comparing the partial cross sections and asymmetry parameters demonstrates the need of correlated calculations. Among the previous calculations in this category, the MBPT approximation is the generally rather successful in reproducing the general trend of the subshell photoionization features over the continuum energy range and the resonant excitation regions: The MBPT results come fairly close to the continuum values of the partial cross sections, even though they do not always reproduce the energy dependences correctly. The RHF results are in good agreement with the experimental data only for the absolute $2s$ cross section and for the angular distribution parameter of $2p$ photoelectrons. Our R-matrix results (in the L form) are too low for the absolute values of the partial cross sections, but show usually good agreement with the measurements for the branching ratios as do the MBPT-3 calculations. Over the autoionization resonance region, only our R-matrix and the recent MBPT calculations reproduce correctly the behavior of the partial cross sections.

The present *ab initio* close-coupling and R-matrix calculations start from a CI description of the target involving 39 states whose energies are well reproduced. Our calculations reproduce correctly the energy dependence of most of the partial cross sections, particularly over the resonance region. The absolute values of our theoretical results are below the experimental values, but our L results lie usually within the experimental error bars. This agreement confirms that results obtained using the length formulation are more reliable in *ab initio* R-matrix calculations. Differences between our length and velocity forms indicate some inconsistencies in their contribution to the general R-matrix equation (10) and a loss of numerical accuracy. The present calculations include core polarization via a CI with ns, np, and nd ($n<4$) orbitals and could be improved by including the remaining core polarization via a CI polarized orbital [63].

On the experimental side, our results demonstrate that there is an urgent need to measure again, with better accuracy, the total photoabsorption cross section. Interferometry techniques could be applied successfully to this aim. In addition, experiments with better resolution are also needed in order to determine the values of the *individual* partial photoionization cross sections and to study with improved photon flux the $2p^4nln'l'$ and $2s2p^6nl$ correlation satellites.

ACKNOWLEDGMENTS

V.K. and F.J.W. acknowledge gratefully the encouraging discussions on this topic with Hugh P. Kelly. We thank Dr. Eissner for his participation at the very first stage of this work and his continued interest. The help of C. Marinelli, T. Menzel, T. Morgan, J. Novak, M. Pahler, M. Richter, and A. S. Schlachter, in taking part of the measurements, is gratefully acknowledged. We would like to thank also M. Berland and D. Huissier for preparing the figures shown in this paper. The experiments were performed at the Laboratoire pour l'Utilisation du Rayonnement Electromagnétique (LURE) in Orsay. We thank the technical staff of Super ACO at LURE for operating the storage ring. The computations were carried out on the RISC/6000/340 workstation at Nice Observatory, on the CRAY-YMP/2*E* (IMT Marseille), and partly on the Cray C98 (IDRIS, Orsay). The experimental program was supported by the Centre National de la Recherche Scientifique and the Ministère de l'Enseignement Supérieur. Partial support was also given by the EU Human Capital and Mobility Program under Contract No. CMRX-CT93-061. A.H. acknowledges support by the URA 1362 du CNRS at the Nice Observatory.

[1] G. Mehlman, J. W. Cooper, and E. B. Saloman, Phys. Rev. A **25**, 2113 (1982).

[2] K. Codling, J. R. Hamley, and J. B. West, J. Phys. B **10**, 2791 (1977).

[3] A. von dem Borne, F. Federmann, M. K. Lee, and B. Sonntag, J. Phys. B **28**, 2591 (1995).

[4] F. J. Wuilleumier and M. O. Krause, Phys. Rev. A **10**, 242 (1974); J. Electron Spectrosc. Relat. Phenom. **15**, 15 (1979).

[5] J.-M. Bizau and F. J. Wuilleumier, J. Electron Spectrosc. Relat. Phenom. **71**, 205 (1979).

[6] H. W. Wolff, K. Radler, B. Sonntag, and R. Haensel, Z. Phys. **257**, 353 (1972).

[7] D. Cubaynes, J.-M. Bizau, F. J. Wuilleumier, B. Carré, and F. Gounand, Phys. Rev. Lett. **63**, 2460 (1989).

[8] D. Cubaynes, J.-M. Bizau, M. Richter, and F. J. Wuilleumier, Europhys. Lett. **14**, 747 (1991).

[9] M. Richter, J.-M. Bizau, D. Cubaynes, T. Menzel, F. J. Wuilleumier, and B. Carré, Europhys. Lett. **12**, 35 (1990).

[10] J. McGuire, Sandia Laboratory Research Report No. SC-RR-721, 1970 (unpublished).

[11] M. Ya Amusia, N. A. Cherepkov, I. Pavlin, V. Radojevic, and Dj Zivanovic, in *Abstracts of the Fourth International Conference on Atomic Physics*, edited by J. Kowalski and H. G. Weber (Universität, Heidelberg, Heidelberg, 1974), p. 328.

[12] M. Ya Amusia and N. A. Cherepkov, Case Stud. At. Phys. **5**, 47 (1975).

[13] M. Ya Amusia, N. A. Cherepkov, I. Pavlin, V. Radojevic, and Dj Zivanovic, J. Phys. B **10**, 1413 (1977).

[14] C. E. Theodosiou and W. Fielder, Jr., J. Phys. B **15**, 4113 (1982).

[15] S. Krummacher, V. Schmidt, J.-M. Bizau, D. L. Ederer, P. Dhez, and F. J. Wuilleumier, J. Phys. B **15**, 4363 (1982).

[16] T.-N. Chang and Y. S. Kim, J. Phys. B **15**, L835 (1982).

[17] E. M. Isenberg, S. L. Carter, H. P. Kelly, and S. Salomonson, Phys. Rev. A **32**, 1472 (1985).

[18] B. I. Craig and F. P. Larkins, J. Phys. B **18**, 3569 (1985); **18**, 3713 (1985).

[19] A. Z. Msezane, W. Armstrong-Mensah, and J. Niles, Phys. Rev. A **42**, 1286 (1990).

[20] S. S. Tayal, A. Z. Msezane, and S. T. Manson, Phys. Rev. A **49**, 956 (1994).

[21] K. A. Berrington, P. G. Burke, K. Butler, M. J. Seaton, P. J. Storey, K. T. Taylor, and Yu Yan, J. Phys. B **20**, 6379 (1987).

[22] J. C. Liu and Z. W. Liu, J. Phys. B **27**, 4531 (1994).

[23] H. Saha, Phys. Rev. A **50**, 3157 (1994).

[24] L. VoKy, H. E. Saraph, W. Eissner, Z. W. Liu, and H. P. Kelly, Phys. Rev. A **46**, 3945 (1992).

[25] F. J. Wuilleumier, M. Y. Adam, P. Dhez, N. Sandner, V. Schmidt, and W. Mehlhorn, Phys. Rev. A **16**, 646 (1977).

[26] V. Schmidt, Phys. Lett. **45A**, 63 (1973).

[27] J. A. R. Samson and A. F. Starace, J. Phys. B **8**, 1806 (1974).

[28] M. Ya Amusia, in *Vacuum Ultraviolet Radiation Physics*, Proceedings of the Tenth VUV Conference, edited by F. J. Wuilleumier, Y. Petroff, and I. Nenner (World Scientific, Singapore, 1993), pp. 3–20.

[29] C. E. Moore, *Atomic Energy Levels*, Natl. Bur. Stand. (U.S.) Circ. No. 467 (U.S. GPO, Washington, DC, 1949), Vol. I.

[30] H. Aksela, A. Ausmees, O.-P. Sairanen, S. J. Osborne, A. Naves de Brito, A. Kivimäki, J. Jauhiainen, S. Svensson, and S. Aksela, Phys. Rev. Lett. **73**, 2031 (1994).

[31] D. Ederer (private communication).

[32] B. Rouvellou, J.-M. Bizau, D. Cubaynes, L. Journel, and F. J. Wuilleumier, J. Electron Spectrosc. Relat. Phenom. **76**, 237 (1995).

[33] W. Ong, S. T. Manson, H. K. Tseng, and R. H. Pratt, Phys. Lett. **69A**, 319 (1979).

[34] D. L. Dehmer (private communication).

[35] A. Hibbert, M. Mohan, and M. LeDourneuf, At. Data Nucl. Data Tables **53**, 23 (1993).

[36] A. Hibbert, Comput. Phys. Commun. **9**, 141 (1975).

[37] E. Clementi and C. Roetti, At. Data Nucl. Data Tables **14**, 177 (1974).

[38] L. VoKy, A. Hibbert, L. Journel, B. Rouvellou, D. Cubaynes, J.-M. Bizau, and F. J. Wuilleumier (unpublished).

[39] W. C. Martin and R. Zalubas, J. Phys. Chem. Ref. Data **10**, 153 (1981).

[40] E. Breuckmann, W. Mehlhorn, and W. Schmitz, J. Phys. B **10**, 3135 (1977).

[41] K. A. Berrington, P. G. Burke, M. Le Dourneuf, W. D. Robb, K. T. Taylor, and L. VoKy, Comput. Phys. Commun. **14**, 367 (1978).

[42] C. Froese-Fischer, Can. J. Phys. **54**, 1465 (1976).

[43] E. Biemont, Astron. Astrophys., Suppl. Ser. **31**, 285 (1978).

[44] K. Butler and C. Mendoza, J. Phys. B **16**, L707 (1983).

[45] U. Fano and D. Dill, Phys. Rev. A **6**, 185 (1972).

[46] M. Le Dourneuf, L. VoKy, and C. Zeippen, J. Phys. B **12**, 2449 (1979).

[47] F. Herman and S. Skillman, *Atomic Structure Calculations* (Prentice-Hall, Englewood Cliffs, NJ, 1963).

[48] F. J. Wuilleumier, L. Journel, B. Rouvellou, D. Cubaynes, J.-M. Bizau, Z. W. Liu, J. C. Liu, M. Richter, P. Sladeczek, K.-H. Selbman, and P. Zimmermann, Phys. Rev. Lett. **73**, 3074 (1994).

[49] B. Rouvellou, L. Journel, J. M. Bizau, D. Cubaynes, F. J. Wuilleumier, M. Richter, K.-H. Selbmann, P. Sladeczek, and P. Zimmermann, Phys. Rev. A **50**, 4868 (1994).

[50] R. E. La Villa, G. Mehlman, and E. B. Saloman, J. Phys. B **14**, L1 (1981).

[51] J.-P. Connerade, W. R. S. Garton, and M. W. D. Mansfield, Astrophys. J. **165**, 203 (1971).

[52] T. Aberg, in *Photoionization and Other Probes of Many-Electron Interactions*, edited by F. J. Wuilleumier (Plenum, New York, 1976), p. 49.

[53] J. C. Liu, X. D. Yang, Y. S. Cheng, and J. Chen, J. Phys. B **29**, L681 (1996).

[54] M. Ya Amusia, V. K. Ivanov, N. A. Cherepkov, and L. V. Chernysheva, Phys. Lett. **40A**, 15 (1972).

[55] F. J. Wuilleumier and M. O. Krause, in *Abstracts of the Eight International Conference on the Physics of Electronic and Atomic Collisions, Belgrade, 1973*, edited by B. C. Čobić and M. V. Kurepa (Institute of Physics, Belgrade, 1973), p. 569.

[56] J. Scofield, Lawrence Livermore Laboratory Report No. 51326, 1973 (unpublished).

[57] D. S. Kennedy and S. T. Manson, Phys. Rev. A **5**, 227 (1972).

[58] K. Codling, R. G. Houlgate, J. B. West, and P. R. Woodruff, J. Phys. B **9**, L83 (1976).

[59] P. G. Burke and Taylor, J. Phys. B **8**, 2620 (1975).

[60] H. Derenbach, R. Malutzki, and V. Schmidt, Nucl. Instrum.

Methods Phys. Res. **208**, 845 (1983).

[61] S. T. Manson, Adv. Electron. Electron Phys. **41**, 73 (1976); **44**, 1 (1977).

[62] B. Rouvellou, J.-M. Bizau, D. Cubaynes, J. Novak, M. Pahler, L. Journel, F. J. Wuilleumier, N. Berrah, L. VoKy, P. Faucher, and A. Hibbert, Phys. Rev. Lett. **75**, 33 (1995).

[63] L. VoKy, M. Le Dourneuf, and P. G. Burke, J. Phys. B **9**, 1065 (1976).